A NEW INFRARED COLOR CRITERION FOR THE SELECTION OF $0 < z < 7$ AGNs: APPLICATION TO DEEP FIELDS AND IMPLICATIONS FOR *JWST* SURVEYS

H. Messias[1,2], J. Afonso[1], M. Salvato[3,4], B. Mobasher[5], and A. M. Hopkins[6]

[1] Centro de Astronomia e Astrofísica da Universidade de Lisboa, Observatório Astronómico de Lisboa, Tapada da Ajuda, P-1349-018 Lisboa, Portugal; hmessias@oal.ul.pt

[2] Departamento de Astronomía, Av. Esteban Iturra 6to piso, Facultad de Ciencias Físicas y Matemáticas, Universidad de Concepción, Chile

[3] Max-Planck Institute for Extraterrestrial Physics, Giessenbachstrasse 1, D-85748 Garching, Germany

[4] Excellence Cluster, Boltzmann Strasse 2, D-85748 Garching, Germany

[5] Department of Physics and Astronomy, University of California, 900 University Avenue, Riverside, CA 92521, USA

[6] Australian Astronomical Observatory, P.O. Box 296, Epping, NSW 1710, Australia

ABSTRACT

It is widely accepted that observations at mid-infrared (mid-IR) wavelengths enable the selection of galaxies with nuclear activity, which may not be revealed even in the deepest X-ray surveys. Many mid-IR color–color criteria have been explored to accomplish this goal and tested thoroughly in the literature. Besides missing many low-luminosity active galactic nuclei (AGNs), one of the main conclusions is that, with increasing redshift, the contamination by non-active galaxies becomes significant (especially at $z \gtrsim 2.5$). This is problematic for the study of the AGN phenomenon in the early universe, the main goal of many of the current and future deep extragalactic surveys. In this work new near- and mid-IR color diagnostics are explored, aiming for improved efficiency—better completeness and less contamination—in selecting AGNs out to very high redshifts. We restrict our study to the *James Webb Space Telescope* wavelength range (0.6–27 μm). The criteria are created based on the predictions by state-of-the-art galaxy and AGN templates covering a wide variety of galaxy properties, and tested against control samples with deep multi-wavelength coverage (ranging from the X-rays to radio frequencies). We show that the colors $K_s - [4.5]$, $[4.5] - [8.0]$, and $[8.0] - [24]$ are ideal as AGN/non-AGN diagnostics at, respectively, $z \lesssim 1$, $1 \lesssim z \lesssim 2.5$, and $z \gtrsim 2.5$–3. However, when the source redshift is unknown, these colors should be combined. We thus develop an improved IR criterion (using K_s and IRAC bands, KI) as a new alternative at $z \lesssim 2.5$. KI does not show improved completeness (50%–60% overall) in comparison to commonly used Infrared Array Camera (IRAC) based AGN criteria, but is less affected by non-AGN contamination (revealing a >50%–90% level of successful AGN selection). We also propose KIM (using K_s, IRAC, and MIPS 24 μm bands, KIM), which aims to select AGN hosts from local distances to as far back as the end of reionization ($0 < z \lesssim 7$) with reduced non-AGN contamination. However, the necessary testing constraints and the small control-sample sizes prevent the confirmation of its improved efficiency at $z \gtrsim 2.5$. Overall, KIM shows a ~30%–40% completeness and a >70%–90% level of successful AGN selection. KI and KIM are built to be reliable against a ~10%–20% error in flux, are based on existing filters, and are suitable for immediate use.

Key words: galaxies: active – galaxies: high-redshift – infrared: galaxies

Online-only material: color figures

1. INTRODUCTION

The active galactic nucleus (AGN) phenomenon in galaxies is currently the focus of a substantial amount of attention, due to its role in altering the path of galaxy evolution (e.g., Granato et al. 2004; Springel et al. 2005; Croton et al. 2006; Hopkins et al. 2006; Bower et al. 2006; Somerville et al. 2008). The quest to find these sources and the techniques used in identifying them are constantly shaping our understanding of the underlying physics of AGNs, which are currently believed to be the result of mass accretion onto supermassive black holes at the very centers of galaxies (e.g., Laor 1999; Melia & Falcke 2001). To identify AGNs, a myriad of techniques has been developed, spanning essentially the full electromagnetic spectrum (e.g., X-rays, Szokoly et al. 2004; optical, Richards et al. 2002; infrared, see references below; radio, Tielens et al. 1979; Chambers et al. 1996).

A wide variety of both intrinsic and observational effects make the identification of large, statistically robust, but also complete and reliable, populations of AGN galaxies challenging. Such effects encompass obscuration, accretion rate,

variability, host galaxy light, viewing angle, and more. Different aspects of AGN radiation may be observed across the entire electromagnetic spectrum (from direct light at high energies to synchrotron radiation dominating at radio frequencies; Treister & Urry 2012). It is common, though, to observe and analyze aspects of AGN activity limited to only one spectral regime. This has been verified in extreme radio sources (Afonso et al. 2006; Simpson et al. 2006; Morganti et al. 2011; Norris et al. 2011) and in some X-ray sources (e.g., Loewenstein et al. 2001; Ho et al. 2003; Maiolino et al. 2003; Polletta et al. 2006). These specific sources show an ultraviolet-to-infrared spectrum with no evidence for AGN activity, and some of these AGNs may not even present any counterpart at those wavelengths (as a result of, for instance, extreme obscuration). Even more generally, there is strong evidence for a large population of obscured AGNs, which still remain unidentified at high-energy spectral bands (e.g., Comastri et al. 2001; Ueda et al. 2003; Gilli 2004; Worsley et al. 2004, 2005; Treister & Urry 2005; Martínez-Sansigre et al. 2005; Draper & Ballantyne 2009). If large dust column densities are the driver for such extreme obscuration (instead of just gas), then infrared (IR) wavelengths, at which

the obscuring dust emits, are an obvious choice in the search for such extreme objects.

Based on data from the *Infrared Astronomical Satellite* (*IRAS*; Neugebauer et al. 1984), de Grijp et al. (1985) and Miley et al. (1985) realized that simple spectral-index or color–color diagnostics could be efficient ways to select Seyfert- and QSO-type galaxies. More recently, with the launch of *Spitzer* (Werner et al. 2004), the same techniques were applied at the shorter wavelengths (3.6–8 μm) of the Infrared Array Camera (IRAC; Fazio et al. 2004), where hotter dust temperatures are probed. Lacy et al. (2004, 2007, L07), Hatziminaoglou et al. (2005), and Stern et al. (2005, S05) proposed different IRAC color–color plots to select AGNs (see also Sajina et al. 2005), while Alonso-Herrero et al. (2006) and Donley et al. (2007) proposed spectral-index diagnostics to select sources revealing power-law ($f \propto \nu^\alpha$) spectral energy distributions (SEDs) characteristic of AGNs (Neugebauer et al. 1979; Elvis et al. 1994; Ivezić et al. 2002). Later, by comparison of the optical spectral regime with IR wave bands, other techniques were proposed. Either through SED fitting (Daddi et al. 2007) or extreme $R - [24]$ color cuts at different 24 μm fluxes (Polletta et al. 2008; Dey et al. 2008; Fiore et al. 2008; Donley et al. 2010), the selected galaxies are too red and bright for a normal star-forming SED, and hence indicative of AGN activity.

However, some critical shortcomings have been highlighted especially regarding the IRAC color–color AGN selection technique (e.g., Barmby et al. 2006; Donley et al. 2008, 2012; Eckart et al. 2010). Having been developed based on the shallow first-generation IRAC surveys, these techniques fail in deeper IRAC surveys, where higher redshift non-AGN sources pollute the adopted selection criteria (Barmby et al. 2006; Papovich et al. 2006; Donley et al. 2008, 2012; Messias et al. 2010). Also, this technique is strongly biased against selecting low-luminosity AGNs (Treister et al. 2006; Cardamone et al. 2008; Donley et al. 2008, 2012; Eckart et al. 2010; Petric et al. 2011), an evolutionary phase where AGNs are believed to spend most of their lifespan (e.g., Hopkins et al. 2005, 2006; Fu et al. 2010). Furthermore, while the IR selection techniques return a variety of AGN populations, there seems to be a bias toward the selection of unobscured over obscured sources (Stern et al. 2005; Donley et al. 2007; Cardamone et al. 2008; Eckart et al. 2010), which, strikingly, is the opposite of the goal that drives IR AGN selection in the first place.

More recently, alternative diagnostics have been proposed, either tuned to specific samples (e.g., Garn et al. 2010; Messias et al. 2010; Donley et al. 2012) or to newly available filter sets (Assef et al. 2010), or in combination with other techniques (Richards et al. 2009; Edelson & Malkan 2012). Such work is crucial and the quest for revised and/or improved color–color criteria should continue, as it is important to identify key filter sets in order to maximize survey efficiency, as well as current (e.g., Salvato et al. 2009, 2011; Hainline et al. 2011; Pozzi et al. 2012) and future SED fitting procedures aiming to break down the strong degeneracy between AGN and non-AGN SEDs.

In this work, we explore new IR color selections with the goal to achieve improved efficiency (better completeness and less non-AGN contamination). In Section 2, different possibilities for the mechanisms behind the IR emission are discussed, and the new criteria are presented in Section 3. A series of tests of these new criteria are explored in Section 4 using a broad set of deep multi-wavelength control samples (selected at wavelengths ranging from X-ray to radio). Implications for and expectations from *James Webb Space Telescope* (*JWST*) surveys
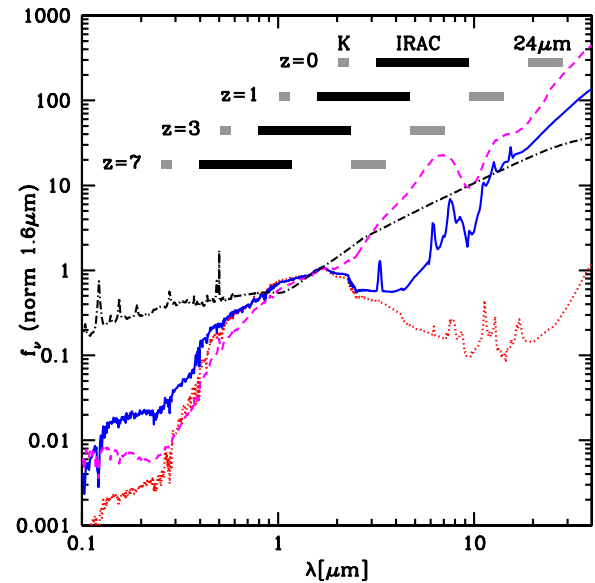
Figure 1. Examples of galaxy templates taken from the SWIRE Template Library (Polletta et al. 2007) and flux normalized at 1.6 μm: S0 (early-type galaxy, red dotted line), M82 (starburst galaxy, blue solid line), IRAS 19254−7245 (a hybrid source, magenta dashed line), and a type-1 QSO (AGN, black dot-dashed line). The shaded regions show what rest-frame wavelength the *K*, IRAC, and MIPS 24 μm filters will be observing depending on the redshift. (A color version of this figure is available in the online journal.)

are highlighted in Section 5, followed by the conclusions of this work in Section 6.

Throughout this paper we use the AB magnitude system,[7] assuming a ΛCDM model with $H_0 = 70$ km s^{-1} Mpc^{-1}, $\Omega_M = 0.3$, and $\Omega_\Lambda = 0.7$.

2. DISTINGUISHING AGNs FROM NON-AGN IR CONTRIBUTIONS

The SEDs of stellar and/or star formation (SF) dominated systems (henceforth referred to as normal galaxy SEDs) have some distinctive characteristics, allowing the separation of this population from AGN host galaxies through the use of IR colors alone. Figure 1 illustrates a few examples using galaxy templates taken from the SWIRE Template Library (Polletta et al. 2007). In normal galaxy SEDs, a dip in the 1–6 μm rest-frame range is expected. The overall blackbody emission from the stellar population combined with the minimum in the opacity of the H$^-$ ion in stellar photospheres peaks at $\sim$1.6 μm, which is generally observed, as is the CO absorption at 2.35–2.5 μm from red supergiants. Emission from hot dust surrounding stars in the asymptotic giant branch phase is expected in young systems ($\lesssim$1 Gyr) and is expected to peak at 2–5 μm (Sajina et al. 2005; Maraston 2005; Henriques et al. 2011). Furthermore, the strength of the polycyclic aromatic hydrocarbon (PAH) features, seen mostly beyond 6 μm, increases with SF activity and metallicity (Calzetti et al. 2007; Engelbracht et al. 2008; Hunt et al. 2010). It is in this spectral region (1–6 μm) that the difference between normal galaxies and AGN-dominated SEDs is the greatest. The existence of an AGN is frequently accompanied by a power-law continuum ($f_\nu \propto \nu^\alpha$; e.g.,

---

[7] When necessary the following relations are used: (*K*, [3.6], [4.5], [5.8], [8.0])$_{AB}$ = (*K*, [3.6], [4.5], [5.8], [8.0])$_{Vega}$ + (1.841, 2.79, 3.26, 3.73, 4.40) (Roche et al. 2003, and http://spider.ipac.caltech.edu/staff/gillian/cal.html).

Neugebauer et al. 1979; Elvis et al. 1994; Ivezić et al. 2002) rising in flux beyond ∼1 μm. This is a consequence of X-ray-to-optical AGN radiation being reprocessed to IR wavelengths by dust surrounding the central region of an active galaxy (Sanders et al. 1989, 1999; Pier & Krolik 1992). This feature, being different from the dip observed in normal galaxy SEDs, is unique for AGN hosts and enables their selection through SED inspection.

2.1. The Template Set

The templates used throughout this paper come from published work as follows: 10 templates covering early to late galaxy types, five starbursts, four hybrids,[8] and six AGNs, all from Polletta et al. (2007); nine starburst ultraluminous IR galaxies (ULIRGs) from Rieke et al. (2009); one blue starburst and 18 hybrid SEDs from Salvato et al. (2009); and one extremely obscured hybrid from Afonso et al. (2001).

All templates have been fully characterized in the papers which introduce them (see above). We assume that they sample adequately the color–z space, based on the results by Salvato et al. (2009, 2011). In these works, the templates above (except those from Afonso et al. 2001 and Rieke et al. 2009) were used to compute reliable photometric redshift estimates reaching an accuracy of $\sigma_{\Delta z/(1+z_{\rm spec})} \sim 0.015$, where $\Delta z = |z_{\rm spec} - z_{\rm phot}|$ for both bright, nearby objects and faint, high-z sources ($z < 5.5$). By further adopting the models from Afonso et al. (2001) and Rieke et al. (2009), the whole template set aims to account for a wide range of mixtures between SF and AGN emission in galaxy SEDs and their evolution across cosmic time, as evidenced by observations (e.g., Farrah et al. 2007; Papovich et al. 2007; Rigby et al. 2008; Pope et al. 2008; Fiore et al. 2008; Donley et al. 2010; Fu et al. 2010; Elbaz et al. 2011). This is a valid assumption given that local templates are successful in fitting some of the most extreme high-redshift sources (for instance, the case of Arp220 as a local analog of HR10, an extremely red galaxy at $z = 1.44$, Hu & Ridgway 1994 and Elbaz et al. 2002; or M82 as an analog for SF-dominated submillimeter galaxies, SMGs, Pope et al. 2008).

Five ULIRGs (IRAS sources 12112+0305, 14348−1447, 17208−0018, 20551−4250, and 22491−1808) which were previously considered as pure starbursts in the literature, are labeled as hybrid sources in this work. This is based on the findings by Veilleux et al. (2009) and the review by Sani & Nardini (2012), where IR spectroscopy is shown to reveal a significant AGN contribution (6%–30% at 8–1000 μm, 8%–40% at 5–8 μm) in these ULIRGs.

Table 1 lists the adopted template set. The SED templates are organized in four groups: (1) early- to late-type galaxies, (2) starbursts, (3) hybrids, and (4) AGNs. The following investigation will focus on how these groups populate near-to-mid IR color–color spaces, aiming to separate the AGN/hybrid population, (3) and (4) above, from normal galaxies, i.e., (1) and (2).

3. THE NEW APPROACH

3.1. An Enhanced Wedge Diagram: The KI Criterion

In Figure 2, the color tracks (spanning the range $0 < z < 7$) for the template SEDs considered are presented on the L07 (left plot) and S05 (right plot) criteria color–color spaces.

---

8 By *hybrids* we refer to SEDs simultaneously including stellar/SF and AGN emission.

Table 1
List of Templates

Class	Template	Ref.[a]
Early/late	Ell13	[2]
	Ell2	″
	Ell5	″
	S0	″
	Sa	″
	Sb	″
	Sc	″
	Sd	″
	Sdm	″
	Spi4	″
Starburst	M82	[2]
	Arp 220	″
	NGC 6090	″
	ESO 0320-g030	[4]
	NGC 1614	″
	NGC 2369	″
	NGC 3256	″
	NGC 4194	″
	Zw049.057	″
	CB1_0_LOIII4	[3]
Hybrid	IRAS 12112+0305	[4,5]
	IRAS 14348−1447	″
	IRAS 17208−0018	″[b]
	IRAS 22491−1808	[2,5]
	IRAS 20551−4250	[2,6]
	IRAS 19254−7245	″
	NGC 6240	″
	Seyfert 2.0	″
	Seyfert 1.8	″
	ERO	[1]
	pl_I22491_10_TQSO1_90	[3]
	pl_I22491_20_TQSO1_80	″
	pl_I22491_30_TQSO1_70	″
	I22491_40_TQSO1_60	″
	I22491_50_TQSO1_50	″
	I22491_60_TQSO1_40	″
	I22491_70_TQSO1_30	″
	I22491_80_TQSO1_20	″
	I22491_90_TQSO1_10	″
	S0_10_QSO2_90	″
	S0_20_QSO2_80	″
	S0_30_QSO2_70	″
	S0_40_QSO2_60	″
	S0_50_QSO2_50	″
	S0_60_QSO2_40	″
	S0_70_QSO2_30	″
	S0_80_QSO2_20	″
	S0_90_QSO2_10	″
AGN	Mrk 231	[2]
	BQSO1	″
	QSO1	″
	TQSO1	″
	QSO2	″
	Torus	″

Notes.
[a] Reference work from which the template was retrieved, and, if present, reference work revealing the presence of hidden or non-dominant AGNs (right column): [1] Afonso et al. 2001; [2] Polletta et al. 2007; [3] Salvato et al. 2009; [4] Rieke et al. 2009; [5] Veilleux et al. 2009; [6] Sani & Nardini 2012.
[b] Veilleux et al. (2009) do not present results for IRAS 17208−0018 specifically, but Rieke et al. (2009, the work where that template comes from) use *Spitzer*-IRS spectroscopy on IRAS 22491−1808 (studied by Veilleux et al. 2009) to complete ISO observations on IRAS 17208−0018, invoking similarities between the two in the 5–11 μm range, where the analysis by Veilleux et al. (2009) is done.
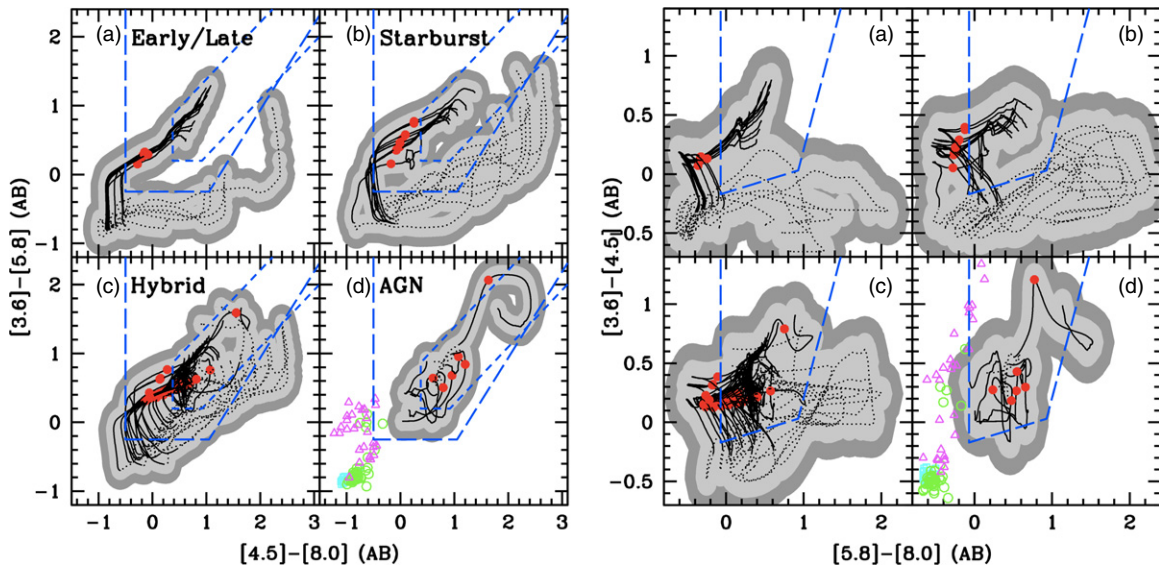
Figure 2. Model color tracks displayed in the L07 (left plot) and S05 (right plot) criterion color–color space. Long-dashed blue lines correspond to the boundaries proposed in those works for the selection of AGNs, while short-dashed blue lines in the left plot correspond to the color boundaries proposed by Donley et al. (2012). Each panel presents a specific group: (a) early/late, (b) starburst, (c) hybrid, and (d) AGNs. The dotted portion of the tracks refers to the $0 < z < 1$ redshift range and the solid to $1 \leqslant z \leqslant 7$. Red circles along the lines mark $z = 2.5$. The light- and dark-gray regions show the photometric scatter due to a magnitude error of, respectively, 0.1 and 0.2 in the bands considered (equivalent to ~10% and ~20% error in flux, respectively). Dwarf stars (Patten et al. 2006) are shown for reference: M-dwarfs appear as open cyan squares, L-dwarfs as open green circles, and T-dwarfs as open magenta triangles to show where these red point-like cool stars appear.
(A color version of this figure is available in the online journal.)

The criterion recently proposed by Donley et al. (2012, D12 henceforward) is also shown in the L07 color–color space, with the caveat that the D12 criterion requires a monotonically increasing red SED in addition to the color cuts shown in the figure. These criteria consider the 3.6–8.0 μm observed frame (the IRAC frame) to select AGN candidates. This is the spectral range where AGN-dominated SEDs are more easily distinguished from normal galaxy SEDs at rest-frame wavelengths, meaning that redshift will play a role in the selection efficiency. In both color–color spaces, the nominal AGN regions encompass most of the AGNs and hybrid tracks for a large range of redshifts, as they were built to do (the D12 criterion focus only on the most SED-dominant AGN).

We note, however, that the use of a very diverse SED template set already shows some shortcomings of these diagnostic plots. In both plots, the two upper panels (early/late and starburst galaxies) show a significant contamination of the nominal AGN region of L07 and S05 (and D12 to a smaller degree) by normal (non-AGN) galaxies. Each criterion is differently affected at different redshifts. Even when ignoring photometric scatter (shaded regions in the figures), one observes non-AGN contamination in at least one criterion throughout the whole $0 < z < 7$ range. This has been noted by previous studies testing the L07, S05, and D12 criteria (Barmby et al. 2006; Donley et al. 2008, 2012; Cardamone et al. 2008), but it is also found for other IR techniques at higher redshifts ($z \gtrsim 2$; e.g., Pope et al. 2008; Donley et al. 2008, 2010; Fadda et al. 2010; Narayanan et al. 2010). While at low redshifts ($z \lesssim 2$–3) the contamination is due to strong PAH emission as well as extreme obscuration differently affecting each IRAC channel, at higher redshifts ($z \gtrsim 2$–3) the contamination is mostly driven by the limitation in observed wavelengths (the IRAC frame, $3.6 < \lambda[\mu m] < 8$). At these redshifts, IRAC bands mostly probe the rest-frame $\lambda \lesssim 1.6 \mu$m, where obscured star-forming systems (frequently identified at those redshifts) present red colors mimicking those of AGNs. The clear implication is that

any AGN criteria restricted to the IRAC frame will never be able to disentangle AGN from non-AGN populations at $z \gtrsim 3$. In Figure 2, the highest redshift where non-AGN templates are restricted to lying outside the S05 and D12 selecting regions is $z \sim 2.5$. At higher redshifts, L07, S05, and D12 are all contaminated to the same degree. At $z < 2.5$, the D12 criterion is the least contaminated (as shown in Donley et al. 2012), but being restricted to such a narrow color–color space it will miss a significant number of low- and intermediate-luminosity AGNs ($\log(L_X[\mathrm{erg\,s^{-1}}]) < 44$). In addition, cool dwarf stars may fall inside or close to the L07 and S05 regions, thus being potential (point-like) contaminants.

In order to enhance these wedge diagrams, one can extend the wavelength coverage to different wave bands. This is obviously outside the IRAC framework behind the original definition of such wedge diagrams, but suits the larger *JWST* wavelength coverage. For instance, by considering shorter wavelengths ($<3 \mu$m), one is probing a spectral region mostly dominated by stellar emission[9] (see Figure 1). Such a scenario is an advantage as we now compare a stellar-dominated wave band with one at longer wavelengths (e.g., the IRAC frame) that has a contribution either from stellar or AGN light. Such a comparison will yield a large color dispersion, which is ideal for the separation of the two types of systems.
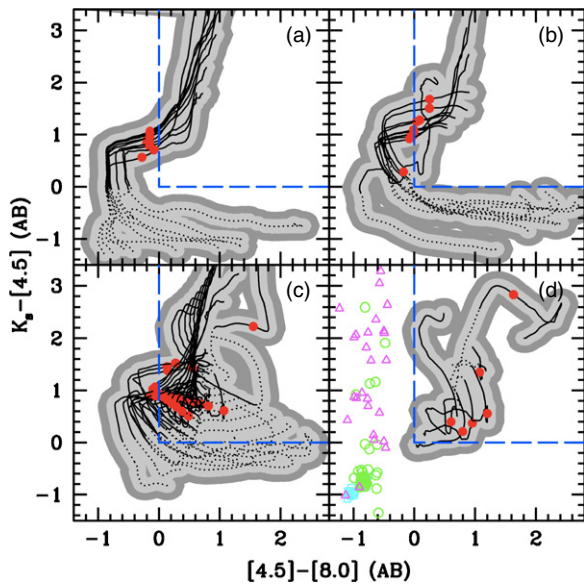
A particularly relevant combination of colors is $K_s - [4.5]$ versus $[4.5] - [8.0]$ (Figure 3). This K_s+IRAC combination, henceforth called the KI criterion, is defined by the following simple conditions:

$$K_s - [4.5] > 0$$

and

$$[4.5] - [8.0] > 0.$$

---

[9] However, AGN emission may also dominate at such short IR wavelengths. See, for example, Assef et al. (2011) and Hainline et al. (2011).

Figure 3. Proposed KI criterion. Symbols and panel definitions are the same as in Figure 2.
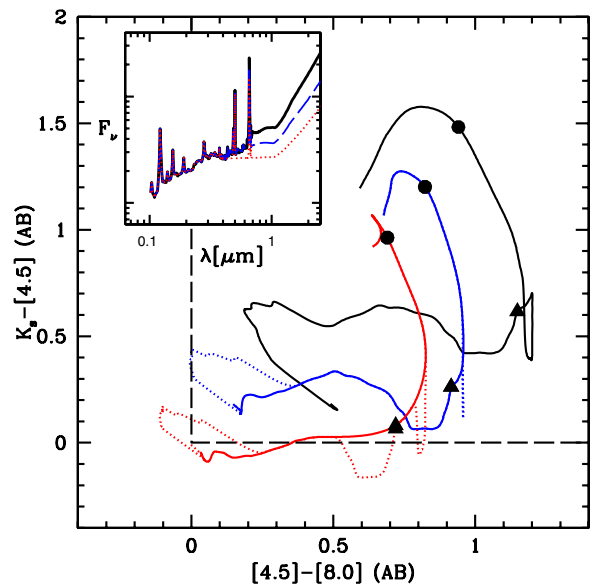
(A color version of this figure is available in the online journal.)

Figure 4. Effects of considering prominent lines in type-1 QSO SED models. The small inset shows three such SEDs originally from Polletta et al. (2007): two updated versions of QSO1 (dashed blue line, now with an Hα line) and BQSO1 (red dotted, now with both Hα and O III lines), and the TQSO1 template (solid black, which already includes Hα and O III lines). On the main panel the original SED model color tracks are shown as solid lines (from top to bottom: TQSO1, QSO1, and BQSO1), whereas the inclusion of strong emission lines produces the deviations given by the dotted segments. Circles and triangles show $z = 1$ and $z = 3$, respectively. The tracks extend from $z = 0$ to $z = 7$.

(A color version of this figure is available in the online journal.)

These color cuts result from a balance between rejecting the non-AGN 10%–20% photometric scatter regions at $z \lesssim 2.5$ and encompassing the pure-AGN color tracks and respective photometric scatter regions. Using a wide variety of templates and taking into account photometric errors we aim to limit possible selection effects resulting from wedges created a posteriori, for example, by using a sample of AGNs spectroscopically confirmed such as in L07 and S05.

Similar to the L07, S05, and D12 criteria, the normal galaxy color tracks contaminate the KI selection region at $z \gtrsim 2.5$. However, the KI contamination by normal galaxies at $z \lesssim 2.5$ appears significantly reduced in comparison to L07 and S05, with no negative effect on the ability to select AGNs (i.e., completeness). By avoiding the 10%–20% error scatter region (light- and dark-gray regions) from starburst templates, the KI boundaries have improved efficiency on faint source classification. Another conceptual improvement of KI is the unbounded upper right AGN region. This avoids the loss of heavily obscured AGNs (with extremely red colors). This is in contrast to the wedges defined in S05, for example, where the Torus template moves out of the selection region at the highest redshifts ($z \gtrsim 4$).

One can also note the usefulness of the simple $K_s - [4.5]$ color in excluding low-redshift normal galaxies: the condition $K_s - [4.5] > 0$ is able to reject a large fraction of the $z < 1$ non-AGN galaxies. Such a property also makes this simple color cut of great use for the study of AGNs and SF co-evolution in the latter half of cosmic history.

Not all the templates in Table 1 take into account prominent emission lines. These may affect the photometry and produce some degree of scatter in the color–color tracks. This is visible in Figure 4 where updated versions (highlighted as dotted lines) of the QSO1 and BQSO1 templates (Polletta et al. 2007) are considered, now with both Hα and O III lines included (visible in the TQSO1 template; Polletta et al. 2007). Although in specific redshift intervals (when a certain emission line is redshifted into a given filter), AGN sources with smaller AGN contribution in the IR (like BQSO1) fall out of the AGN region of the KI

criterion, the bulk of the AGN population is expected to remain inside the KI boundaries.

3.2. Extending to High Redshifts: the KIM Criterion

One serious problem for all criteria investigated so far is the contamination by normal galaxies at $z \gtrsim 2.5$. All four (L07, S05, D12, and KI) fail to disentangle AGN-dominated systems from normal galaxies at those redshifts. To avoid this problem, longer wavelength observed bands should be considered, allowing the observation of the rest-frame $\lambda > 1.6\,\mu$m regime, where AGN emission may dominate, at high redshifts. For this purpose, we extend our study to include the MIPS 24 μm band (see also Sajina et al. 2005).

The use of this wave band for AGN selection has additional shortcomings. Normal galaxies show a wide IRAC–MIPS color range (as a result of different PAH and dust emissions between galaxies), which is further increased by redshift (the PAH features are redshifted out of the 8.0 μm band at low z, but redshifted into the 24 μm band at $z \sim 2$). This results in a considerable color overlap with AGNs, limiting the usefulness of a single IRAC–MIPS color to separate both populations (Lacy et al. 2004; Hatziminaoglou et al. 2005; Cardamone et al. 2008). Nevertheless, some authors have used the MIPS 24 μm band for unique, extreme objects (e.g., the IR-excess technique, Section 4.2) or in single, unconventional situations. For instance, while Garn et al. (2010) use $[8.0] - [24]$ against $[5.8] - [8.0]$ for a $z \sim 0.8$ sample to identify those sources showing AGN activity, Treister et al. (2006) and Messias et al. (2010) use a single $[8.0] - [24]$ color cut at, respectively, $z \sim 2$ and $z > 2.5$ for the same purpose.[10]

---

[10] Ivison et al. (2004) and Pope et al. (2008) also explore $[8.0] - [24]$ against $[4.5] - [8.0]$ to distinguish AGNs from normal galaxies, but in those works only the $[4.5] - [8.0]$ color is effectively used for that purpose.
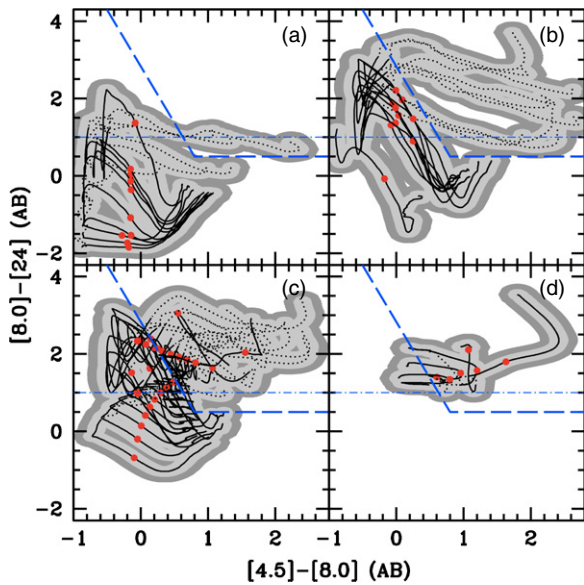
Figure 5. IRAC–MIPS color–color space and the proposed criterion. Symbols and panel definitions are the same as in Figure 2. The dot-dashed horizontal blue line (at $[8.0] - [24] = 1$) refers to a simpler criterion valid at $z \gtrsim 3$, as detailed in the text and illustrated in Figure 6.

(A color version of this figure is available in the online journal.)

Figure 6. The $[8.0]-[24]$ color evolution with redshift. Panel definitions are the same as in Figure 2. The horizontal line shows $[8.0] - [24] = 1$, while the vertical one indicates $z = 3$. At $z > 3$, only AGN-dominated galaxies show $[8.0] - [24] > 1$ colors.

(A color version of this figure is available in the online journal.)

Colors involving the 24 μm band are also usually avoided due to the large wavelength gap between this band and other commonly available MIR bands (usually the *Spitzer*-IRAC bands). At high z (e.g., $z \sim 3$), however, the sampled rest-frame wave bands (2 and 6 μm corresponding to observed 8 and 24 μm, respectively) are not much more separated than the 3.6 and 8.0 μm IRAC bands for nearby galaxies. A different issue is the lower sensitivity and larger point-spread function of the MIPS 24 μm images when compared with those obtained with the IRAC channels, which affects the accuracy of color measurements using this longer wavelength band. Nevertheless, efficient photometry algorithms have been built to overcome these blending problems (Wuyts et al. 2008; Santini et al. 2009).

Figure 5 illustrates a color–color AGN diagnostic proposed for $z \gtrsim 1$, with its boundaries avoiding a 10% photometric error scatter from normal galaxies. The criterion is defined by the following IRAC–MIPS (IM) conditions:
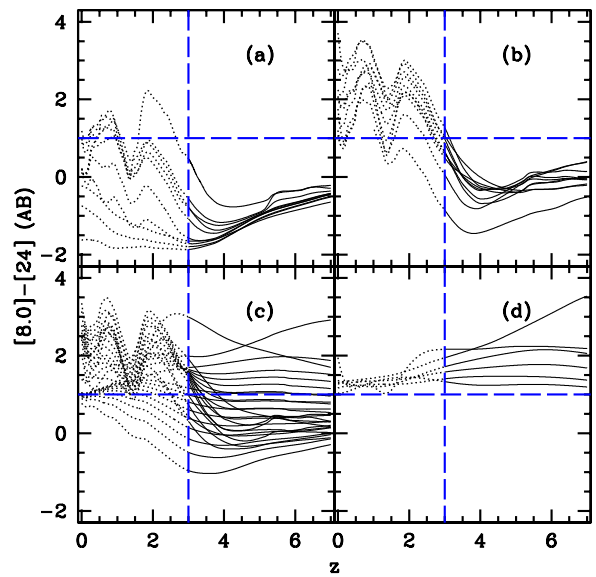
$$[8.0] - [24] > -2.9 \times ([4.5] - [8.0]) + 2.8$$

and

$$[8.0] - [24] > 0.5.$$

One can see that beyond $z \sim 1$, AGN (lower panels) and normal galaxies (upper panels) occupy essentially different regions in the $[8.0]-[24]$ versus $[4.5]-[8.0]$ space. This is of great interest for the characterization of high-redshift galaxy populations, such as Lyman break galaxies (LBGs) and equivalents at $z \gtrsim 2$ (Steidel et al. 2003, 2004; Adelberger et al. 2004), or spectroscopically confirmed high-z galaxies. We note, nevertheless, the incompleteness toward type-1 QSOs at $z \gtrsim 4$–5[11] or type-2 QSOs with strong Hα emission affecting the 4.5 μm band at $z \gtrsim 4.5$ (Figure 4). Note, however, that Mrk231 and torus-type AGNs remain inside the region for the full redshift range studied ($0 < z < 7$).

At low redshifts ($z \lesssim 1$), degeneracy exists in this IM color–color space, with AGNs and normal galaxies occupying the same color–color region. A rejection of low-redshift ($z < 1$) normal/star-forming galaxies would, however, remove this overlap, allowing for a powerful AGN selection criterion to be built. This can be achieved, as noted in the previous section, by using the $K_s - [4.5] > 0$ color cut (Figure 3). This allows the rejection of a large fraction of the $z \lesssim 1$ non-AGN galaxies, with AGNs and hybrid galaxies in this redshift range remaining mostly unaffected.

The IRAC–MIPS (IM) conditions presented above, when considered together with the $K_s - [4.5] > 0$ cut, which implements the rejection of $z < 1$ normal galaxies, define what we will henceforth call the KIM (K_s+IRAC+MIPS) criterion.

We further note from Figure 5 that for $z \gtrsim 3$ essentially all SEDs with $[8.0] - [24] > 1$ are dominated by AGN emission. This happens because in this redshift range, the PAH features dominating a normal galaxy SED are redshifted out of the $MIPS_{24\,\mu m}$ filter. Figure 6 details this behavior, clearly showing that stellar-dominated galaxies at $z \gtrsim 3$ show $[8.0] - [24] < 1$ colors, as described by Messias et al. (2010). Such a color cut, if possible to apply (one has to know the source redshift), allows the recovery of Hα-emitting and/or rest-frame UV/optical blue QSOs expected to leave the IM region at $z \gtrsim 4$–5 (Figure 5).

We acknowledge that by aiming at such a broad redshift range ($0 < z \lesssim 7$) KIM has its shortcomings. For instance, if the goal is to characterize sources at $z \lesssim 1$, the use of $K_s - [4.5]$ allows a reliable selection of AGN hosts avoiding the need for longer wavelength bands. On the other hand, at $z \gtrsim 3$, the $[8.0]-[24]$ color is enough to identify AGN-dominated sources, avoiding the loss of sources undetected at shorter wavelengths. Finally, the $[4.5] - [8.0]$ color is best at intermediate redshifts ($1 \lesssim z \lesssim 2.5$).

However, a redshift estimate is frequently not available (incomplete spectroscopic sample coverage) or is not reliable (photometric redshifts). Particularly for AGN-dominated sources, where a power-law SED is observed, the lack of spectral

features (such as spectrum breaks) makes the photometric red-shift solutions degenerate. In order to avoid such limitations, while still allowing AGN selection up to $z \sim 7$, the KIM criterion may be valuable.

4. TESTING AGAINST MULTI-WAVELENGTH AGN SAMPLES

In the previous section we have proposed:

1. $K_s - [4.5]$ as a useful color for the efficient segregation of the galaxy population into AGN-dominated and normal SEDs at $z \lesssim 1$;
2. KI criterion as an alternative to L07, S05, and D12;
3. KIM (a four-band, three-color criterion) as a diagnostic which, according to the color tracks of the templates used, enables the selection of AGN sources at $0 < z \lesssim 7$ with little contamination by normal galaxies.

This is of great interest as it allows one to trace AGN activity since the epoch of reionization to the current time. The usefulness of these criteria can only be evaluated, however, by pursuing a test with well-characterized control samples. Using various samples for which normal-galaxy and AGN classifications are obtained via other spectral regimes (from X-rays to radio), we can obtain some estimate of the efficiency of the new proposed diagnostics in comparison with commonly used ones.

Because an ideal sample, where *all* the sources are *reliably* split between AGN and non-AGN hosts, does not exist, we will perform these tests using five control samples. First, we use a sample of galaxies from the *Chandra* Deep Field South (CDFS; Giacconi et al. 2001) and another from the Cosmic Evolution Survey (COSMOS; Scoville et al. 2007), both with available AGN/non-AGN classification from X-rays and/or optical spectroscopy. Second, we assemble samples of IR-excess (IRxs) sources (Dey et al. 2008; Fiore et al. 2008; Polletta et al. 2008) found in CDFS and COSMOS fields. The QSO sample from the Sloan Digital Sky Survey (SDSS; Schneider et al. 2010), reaching $z \sim 6$, is also considered for the testing, as well as the high-z radio galaxy (HzRG) sample from Seymour et al. (2007). The first two samples (X-ray/optical selected in CDFS and COSMOS) allow for an indication of the completeness and non-AGN contamination of the IR AGN selection criteria, while the AGN samples (IRxs sources, SDSS QSOs, and HzRGs) will allow for independent measures of their completeness up to the highest redshifts.

In the following sections, completeness ($\mathcal{C}$) is defined as the fraction of the AGN population which a given IR criterion selects (AGN$_{\rm SEL}$/AGN$_{\rm TOT}$), while reliability ($\mathcal{R}$) refers to the fraction of the IR sources selected by a given criterion which are "true" AGNs (AGN$_{\rm SEL}$/$N_{\rm SEL}$, where $N_{\rm SEL}$ = AGN$_{\rm SEL}$+non-AGN$_{\rm SEL}$).

4.1. The CDFS and COSMOS Samples

We have selected 2287 galaxies from the MUSIC/CDFS catalog (Grazian et al. 2006; Santini et al. 2009) and 7217 from COSMOS (Ilbert et al. 2009) with an X-ray classification (based on source luminosity and spectral slope) and/or a good quality[12] optical spectroscopic classification. Whenever a spectroscopic redshift was not available, the photometric estimates by Luo et al. (2010) and Salvato et al. (2011) were adopted.

The IR data used for the MUSIC catalog come from Vandame (2002) and M. Dickinson et al. (in preparation), and that for COSMOS comes from Sanders et al. (2007), Le Floc'h et al. (2009), and McCracken et al. (2010). Regarding the X-rays, the 2 Ms *Chandra* Deep Field South (CDFS; Luo et al. 2008) data were used, as well as the *XMM* data in COSMOS (Cappelluti et al. 2009; Brusa et al. 2010). The X-ray AGN classification is similar to that of Szokoly et al. (2004). There, the X-ray luminosity and hardness ratio (HR) are used to identify the AGN population. The HR is a measure of the source obscuration and is defined as HR $\equiv$ (H$-$S)/(H+S) with H and S being, respectively, the net counts in the hard, 2–8 keV, and soft, 0.5–2 keV, X-ray bands. However, this ratio becomes degenerate with redshift (Eckart et al. 2006; Messias et al. 2010, but also Alexander et al. 2005; Luo et al. 2010), and count measurements depend on array efficiency between telescopes. Hence, we compute for each source the respective column densities ($N_{\rm H}$) using the Portable, Interactive Multi-Mission Simulator[13] (PIMMS, version 3.9k). The soft-band/full-band (SB/FB) and hard-band/full-band (HB/FB) flux ratios[14] were estimated for a range of column densities ($19 < \log(N_{\rm H}[{\rm cm}^{-2}]) < 25$, with steps of $\log(N_{\rm H}[{\rm cm}^{-2}]) = 0.01$), and redshifts ($0 < z < 7$, with steps of $z = 0.01$), considering a fixed photon index, $\Gamma = 1.8$ (Tozzi et al. 2006). The comparison with the observed values results in the estimate of $N_{\rm H}$. However, it is known that this procedure systematically overestimates the intrinsic $N_{\rm H}$. The Appendix discusses this bias and how we attempted to correct it. The final $N_{\rm H}$ value is then used to derive an intrinsic X-ray luminosity. The HR constraint used by Szokoly et al. (2004) (HR = -0.2) is equivalent to $\log(N_{\rm H}[{\rm cm}^{-2}]) = 22$ at $z \sim 0$, and this is the value considered throughout the whole redshift range.

Hence, an X-ray AGN is considered to have $L_X^{\rm int} > 10^{41}$ erg s^{-1} and $N_{\rm H} > 10^{22}$ cm^{-2}, or $L_X^{\rm int} > 10^{42}$ erg s^{-1}. The remaining X-ray detections are regarded as non-AGN sources. The intrinsic X-ray (0.5–10 keV) luminosities are estimated as

$$L_X^{\rm int} = 4\pi \, d_{\rm L}^2 \, f_X^{\rm int} \, (1+z)^{\Gamma-2} \, {\rm erg \, s}^{-1},$$

where $f_X^{\rm int}$ is the obscuration-corrected X-ray flux in the 0.5–10 keV band, and Γ is the observed photon index (when $\log(N_{\rm H}[{\rm cm}^{-2}]) \leqslant 19$) or $\Gamma = 1.8$ (when $\log(N_{\rm H}[{\rm cm}^{-2}]) > 19$). In CDFS, the 0.5–8 keV luminosities are derived using Luo et al. (2008) cataloged 0.5–8 keV fluxes and converted to 0.5–10 keV considering the adopted Γ. For simplicity, the luminosity "int" label is dropped from now on, as we will always be referring to intrinsic luminosities, unless otherwise stated.

Regarding the spectroscopic sample, the AGN sources are those which display broad line features or high-ionization narrow emission lines characteristic of AGN activity (BLAGN or NLAGN, respectively). The remaining sources with a spectroscopic classification are regarded as part of the non-AGN population (e.g., SF galaxies, stars). The NLAGN classification comes from the MUSIC catalog in CDFS and from Bongiorno et al. (2010) in COSMOS.

In both the CDFS and COSMOS final AGN samples, most sources have an X-ray AGN classification (82% and 80%, respectively), and a significant fraction has a spectroscopic AGN classification (21% in CDFS and 55% in COSMOS, the

---

[12] Spectra flagged as 0 (very good) or 1 (good) in the MUSIC catalog, and estimates with >90% probability of being correct in the zCOSMOS catalog.

[13] http://heasarc.nasa.gov/docs/software/tools/pimms.html
[14] The use of ratios based on FB flux instead of the commonly used SB/HB flux ratios allows for an estimate of $N_{\rm H}$ when the source is detected in the FB but no detection is achieved in either the SB or HB.
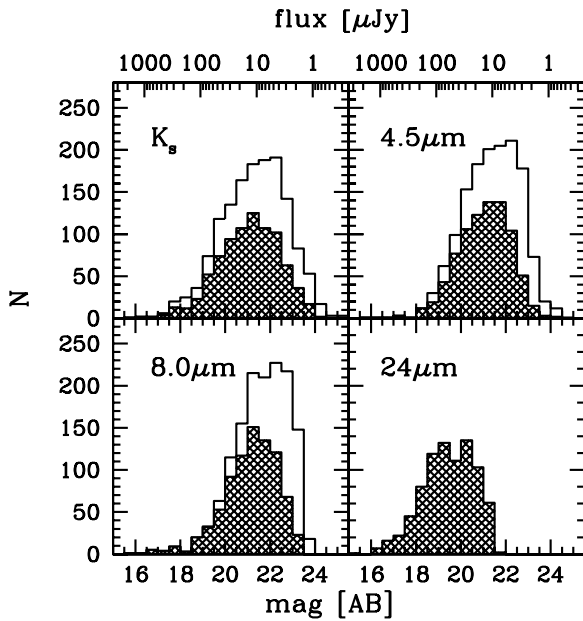
Figure 7. Magnitude distribution of the final CDFS sample with reliable photometry in K_s–IRAC bands (open histogram) and K_s–IRAC–MIPS$_{24\,\mu m}$ (hatched histogram). Each panel refers to the magnitude distribution in the following bands: K_s (upper left), $4.5\,\mu$m (upper right), $8.0\,\mu$m (lower left), and $24\,\mu$m (lower right). Note that in the latter both histograms coincide.

difference resulting from different spectroscopic completenesses between the two surveys).

4.1.1. KI/KIM Efficiency in CDFS

For consistency, we only consider sources having photometry estimates with a flux error smaller than a third of the flux measurement (equivalent to an error in magnitude smaller than 0.36) in all K_s–IRAC bands when testing L07, S05, D12, and KI. This requirement will remove many of the fainter objects, but the final sample is still among the deepest ever used to test these IR criteria. The magnitude distribution of the final sample considered is shown in Figure 7 (see open histograms). Among the 1440 sources composing the final sample, 166 (12%) are classified as AGN hosts (160 in X-rays, 38 through spectroscopy). The sample is further separated into redshift ranges: $0 \leqslant z < 1$, $1 \leqslant z < 2.5$, $2.5 \leqslant z < 4$. The adopted threshold at $z = 2.5$ is based on the discussion in Section 3.1. This results in 801, 535, and 94 sources with K_s–IRAC photometry at $0 \leqslant z < 1$, $1 \leqslant z < 2.5$, and $2.5 \leqslant z < 4$, respectively.

When testing KIM we also require reliable $24\,\mu$m photometry (hatched histograms in Figure 7). However, this requirement restricts the sample to the brightest sources, unavoidably increasing the probability of finding AGN-dominated sources (Brand et al. 2006; Treister et al. 2006; Donley et al. 2008). Although it can be considered a constraint by itself (which improves the criterion efficiency), this results in an unfair comparison of the actual color–color regions. Hence, when comparing KIM to L07, S05, and KI, we consider the sample of 834 sources (460/324/47 at $0 \leqslant z < 1$, $1 \leqslant z < 2.5$, and $2.5 \leqslant z < 4$, respectively) with reliable K_s–IRAC–MIPS$_{24\,\mu m}$ photometry, of which 139 (17%) are classified as AGN hosts.

Tables 2, 3, and 4 summarize the final statistics for the application of each of the IR criteria to the CDFS control sample at different redshift ranges. In order to assess the significance of the results, two types of error are presented:

Table 2
CDFS X-Ray and Spectroscopic $0 \leqslant z < 1$ Control Sample Test

Sample	Criterion	$N_{\rm SEL}$ [a]	AGN [b]	$\mathcal{C}$ [c]	$\mathcal{R}$ [c]
K_s+IRAC	[none]	801	42	...	(5 ± 1)
	L07	105	21	$50(13^2_2)$	$20(5^9_8)$
	S05	26	12	$29(9^5_5)$	$46(16^{15}_{13})$
	D12	5	4	$10(5^2_2)$	$80(54^3_{20})$
	KI	24	12	$29(9^0_0)$	$50(18^{13}_2)$
K_s+IRAC+ MIPS$_{24\,\mu m}$	[none]	460	37	...	(8 ± 1)
	L07	76	18	$49(14^3_0)$	$24(6^6_7)$
	S05	20	11	$30(10^3_5)$	$55(21^5_{16})$
	D12	5	4	$11(6^0_3)$	$80(54^0_{20})$
	KI	17	10	$27(10^0_0)$	$59(23^8_3)$
	KIM	10	7	$19(8^0_0)$	$70(34^0_{20})$

Notes. This table is restricted to the $0 \leqslant z < 1$ CDFS sample. While in the upper group of rows reliable photometry is required—a magnitude error below 0.36—in K_s+IRAC bands, in the lower group of rows we also require reliable 24 μm photometry. The first row in each group refers to the total number of sources with reliable K_s+IRAC (upper group) and K_s+IRAC+24 μm (bottom group) photometry. For reference, the values in parentheses (with the corresponding Poisson error) in the $\mathcal{R}$ column give the overall fraction of identified AGN hosts, equivalent to the $\mathcal{R}$ of a criterion selecting all sources in the field with reliable photometry in the bands considered.
[a] Number of sources selected by a given criterion with an AGN/non-AGN classification from X-rays and/or spectroscopy.
[b] Number of selected sources with an AGN classification, from either the X-rays or optical spectroscopy.
[c] Completeness ($\mathcal{C}$) calculated as AGN$_{\rm SEL}$/AGN$_{\rm TOT}$. Reliability ($\mathcal{R}$) calculated as AGN$_{\rm SEL}$/$N_{\rm SEL}$. Numbers in parenthesis refer, respectively, to the Poisson error and the photometric upper and lower error bars.

Table 3
CDFS X-Ray and Spectroscopic $1 \leqslant z < 2.5$ Control Sample Test

Sample	Criterion	$N_{\rm SEL}$	AGN	$\mathcal{C}$	$\mathcal{R}$
K_s+IRAC	[none]	535	80	...	(15 ± 2)
	L07	170	50	$62(11^6_2)$	$29(5^{12}_8)$
	S05	104	28	$35(8^6_7)$	$27(6^{22}_{13})$
	D12	18	15	$19(5^0_4)$	$83(29^{17}_7)$
	KI	60	32	$40(8^1_4)$	$53(12^{14}_{21})$
K_s+IRAC+ MIPS$_{24\,\mu m}$	[none]	324	61	...	(19 ± 3)
	L07	110	39	$64(13^5_2)$	$35(7^9_6)$
	S05	70	25	$41(10^5_7)$	$36(8^{17}_{15})$
	D12	15	14	$23(7^0_5)$	$93(35^7_9)$
	KI	40	26	$43(10^2_4)$	$65(16^8_{16})$
	KIM	25	16	$26(7^3_3)$	$64(20^{14}_{14})$

Notes. This table is restricted to the $1 \leqslant z < 2.5$ CDFS sample. Table structure and column definitions are the same as in Table 2.
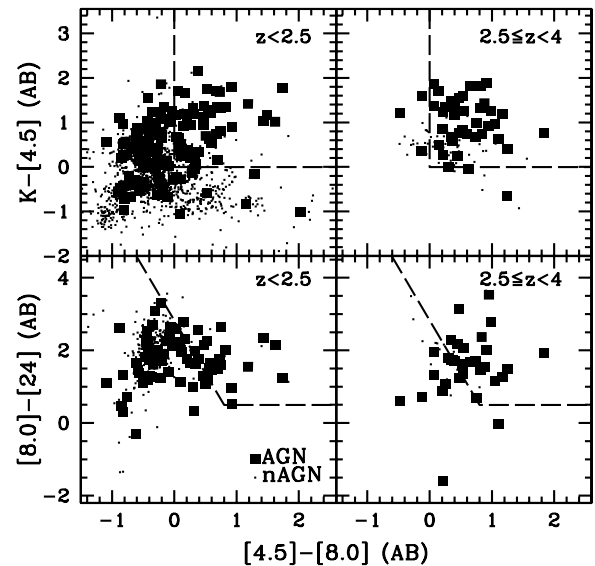
Poisson and photometric. The latter is computed by scattering the source colors between the $\pm 1\sigma$ magnitude errors (which we limited to $< 1/3$ of the flux value) and we evaluate how completeness ($\mathcal{C}$) and reliability ($\mathcal{R}$) vary as a result. However, there is a covariance between observational photometric and Poisson sampling errors, since the samples with the smallest photometric errors are the smallest in number, leading in turn to large sampling errors. Since our approach is based around testing color-space boundaries that have already accounted for generous photometric variation around the SED templates in their definition, the current analysis is primarily limited by

Table 4
CDFS X-Ray and Spectroscopic $2.5 \leqslant z < 4$ Control Sample Test

Sample	Criterion	$N_{\rm SEL}$	AGN	$\mathcal{C}$	$\mathcal{R}$
K_s+IRAC	[none]	94	40	...	(43 ± 8)
	L07	93	40	$100(22_{-5}^{0})$	$43(8_{-2}^{3})$
	S05	54	29	$72(18_{-20}^{10})$	$54(12_{-18}^{23})$
	D12	29	20	$50(14_{-12}^{18})$	$69(20_{-27}^{27})$
	KI	73	36	$90(21_{-5}^{3})$	$49(10_{-7}^{8})$
K_s+IRAC+	[none]	47	33	...	(70 ± 16)
MIPS$_{24\,\mu m}$	L07	47	33	$100(25_{-6}^{0})$	$70(16_{-1}^{2})$
	S05	32	24	$73(20_{-15}^{9})$	$75(20_{-14}^{7})$
	D12	20	17	$52(15_{-9}^{18})$	$85(28_{-11}^{15})$
	KI	41	30	$91(23_{-3}^{0})$	$73(18_{-2}^{4})$
	KIM	24	20	$61(17_{-9}^{12})$	$83(25_{-15}^{9})$

Notes. This table is restricted to the $2.5 \leqslant z < 4$ CDFS sample. Table structure and column definitions are the same as in Table 2.

Figure 8. CDFS sources in KI (upper panels) and KIM (lower panels) color–color spaces, divided into low-z ($z < 2.5$, left panels) and high-z ($2.5 \leqslant z < 4$, right panels) groups. Squares represent AGN hosts (as classified from X-rays or optical spectroscopy), while dots highlight non-AGN sources. The dashed lines in the upper panels refer to the KI criterion, while the dashed lines in the lower panels refer to the IM region proposed in Section 3.2. All sources displayed in the lower panels have $K_s - [4.5] > 0$, as required by the KIM criterion.

sampling (Poisson) errors. In general, the Poisson errors are larger than those that would be inferred from the photometric errors alone, so this approach is also conservative in the sense of erring in favor of the larger uncertainty. The discussion and results presented below are consequently based on a consideration of the Poisson errors associated with the sample sizes being used in the analysis of completeness and reliability.

In the low redshift bin ($0 \leqslant z < 1$), L07 is the most complete (selecting almost 50% of the AGN sample), but the least reliable as well, with less than a fifth of the sample being confirmed AGN hosts. This is understood given the large selection region set by the color constraints of L07 criterion, which despite selecting many AGN hosts (high $\mathcal{C}$) also selects many non-AGN sources (low $\mathcal{R}$). S05, KI, and KIM present almost comparable efficiencies, selecting around a quarter of the AGN population, and with 50%–60% reliabilities. D12 retrieves the lowest $\mathcal{C}$ values (10%, comparable with KIM, see also Section 4.1.2), but at the same time the highest $\mathcal{R}$ values (80%, although with large Poisson errors).

At $1 \leqslant z < 2.5$, L07 is still the criterion that provides the most complete AGN sample, but here it presents an $\mathcal{R}$ value of ∼30%, comparable to that of S05. Both KI and KIM present improved $\mathcal{R}$ levels, with 50%–60% of the sample being confirmed as AGN hosts. The improvement relative to the L07 and S05 criteria in this redshift range appears to be due to the $[4.5] - [8.0]$ color cut used. The D12 criterion is again the criterion that presents the lowest $\mathcal{C}$ (20%) and the highest $\mathcal{R}$ (80%–90%). The D12 criterion is affected by small sample statistics, but it always recovers the highest $\mathcal{R}$ values, supporting the scenario that it is in fact the most reliable of all the criteria tested.

At high z ($2.5 \leqslant z < 4$), the fraction of "true" AGN hosts is already high (43%, increasing to 70% when restricting to the MIPS$_{24\,\mu m}$ detected sample). As a result of the small number of sources (driven by the necessary quality constraints), no conclusion can be drawn regarding $\mathcal{R}$ from this sample at such high redshifts, given that all criteria provide comparable $\mathcal{R}$ results within the uncertainties. However, differences in completeness exist. D12 and KIM show the lowest values ($\mathcal{C} \sim$ 50%–60%), KI and L07 the highest ($\mathcal{C} \sim$ 90%–100%), while S05 gives intermediate values ($\mathcal{C} \sim$ 70%).

One should also note the tendency for S05 and KIM to present the largest range between lower and upper photometric limits. While in KIM this relates to the use of the less sensitive

MIPS$_{24\,\mu m}$ band, the larger photometric error ranges in S05 are due to the use of bands close in wavelength (Figure 2), instead of bands widely separated in wavelength as in L07, KI, and KIM. The large photometric errors found for the D12 criterion are probably related to the small sample statistics (see COSMOS results below, where these errors are close to zero).

Finally, Figure 8 details the application to the CDFS data of KI (upper panels) and KIM (lower panels), separated into redshift bins ($z < 2.5$ and $2.5 \leqslant z < 4$). For this exercise, we have required reliable photometry in the bands needed for KI or KIM. This figure shows that the KI and KIM criteria still miss a significant fraction (around two-thirds) of the AGN population at $z < 2.5$. The high-redshift panels show that most (around three quarters) of the overall population indeed falls inside the KI selection region (in agreement with Figure 3). The low number of blue $[8.0] - [24]$ sources is mainly a result of the photometric quality constraints applied to the sample. Knowing that the MIPS$_{24\,\mu m}$ band is also the less sensitive wave band, at high redshifts, where sources tend to be fainter, blue $[8.0] - [24]$ sources will likely not be detected in the MIPS$_{24\,\mu m}$ band and consequently will be absent from this exercise.

When no redshift estimate is available, the previous analysis, which separates the sample into redshift bins, would not be possible. Table 5 shows the results for the overall CDFS sample with no redshift constraint. The conclusions remain the same: KI and KIM are complete to ∼50% and ∼35% levels, respectively, and both show improved reliability ($\mathcal{R} \sim$ 50%–70%) relative to L07 and S05 (KI and S05 error bars marginally overlap); D12 is less complete (with values comparable to KIM, $\mathcal{C} =$ 25%–30%), but the most reliable ($\mathcal{R} =$ 76%–88%).

4.1.2. KI/KIM Efficiency in COSMOS

The same comparison is now performed for COSMOS. No redshift segregation is applied as there is no classified SF system at $z \gtrsim 1.6$ in this COSMOS sample. Among the 7216 sources

Table 5
CDFS X-Ray and Spectroscopic Control Sample Test

Sample	Criterion	$N_{\rm SEL}$	AGN	$\mathcal{C}$	$\mathcal{R}$
K_s+IRAC	[none]	1440	166	...	(12 ± 1)
	L07	377	115	$69(8_{3}^{4})$	$31(3_{8}^{9})$
	S05	188	73	$44(6_{10}^{7})$	$39(5_{17}^{22})$
	D12	55	42	$25(4_{6}^{5})$	$76(16_{25}^{20})$
	KI	166	84	$51(7_{3}^{1})$	$51(7_{12}^{11})$
K_s+IRAC+	[none]	834	134	...	(16 ± 1)
MIPS$_{24\,\mu m}$	L07	236	93	$69(9_{2}^{3})$	$39(5_{8}^{7})$
	S05	125	63	$47(7_{9}^{5})$	$50(8_{17}^{14})$
	D12	42	37	$28(5_{5}^{4})$	$88(20_{11}^{10})$
	KI	101	69	$51(8_{1}^{1})$	$68(11_{9}^{6})$
	KIM	62	46	$34(6_{4}^{4})$	$74(14_{16}^{10})$

Notes. No redshift cut is considered in this table. Table structure and column definitions are the same as in Table 2.

Table 6
COSMOS X-Ray and Spectroscopic Control Sample Test

Sample	Criterion	$N_{\rm SEL}$	AGN	$\mathcal{C}$	$\mathcal{R}$
K_s+IRAC	[none]	7216	1423	...	(20 ± 1)
	L07	2038	1115	$78(3_{3}^{3})$	$55(2_{9}^{10})$
	S05	1102	921	$65(3_{7}^{5})$	$84(4_{13}^{9})$
	D12	586	573	$40(2_{4}^{5})$	$98(6_{3}^{0})$
	KI	967	881	$62(3_{3}^{4})$	$91(4_{4}^{3})$
K_s+IRAC+	[none]	2641	842	...	(32 ± 1)
MIPS$_{24\,\mu m}$	L07	1087	727	$86(4_{2}^{1})$	$67(3_{5}^{5})$
	S05	701	629	$75(4_{4}^{2})$	$90(5_{4}^{4})$
	D12	464	454	$54(3_{2}^{3})$	$98(6_{0}^{0})$
	KI	643	588	$70(4_{1}^{1})$	$91(5_{2}^{2})$
	KIM	435	398	$47(3_{4}^{3})$	$91(6_{3}^{2})$

Notes. Table structure and column definitions are the same as in Table 2. No redshift range is adopted as there is no classified SF system at $z \gtrsim 1.6$ in the COSMOS sample.

with either a spectral or X-ray classification and adequate K_s–IRAC photometry, 1423 are flagged as AGN hosts by X-ray and spectroscopy criteria. There are 2641 sources with MIPS$_{24\,\mu m}$ detection (842 AGN hosts). Table 6 reports the final statistics on the application of the various diagnostics. Note that 84% of this COSMOS sample is found at $z < 1$, implying that the statistics of this sample will be dominated by those of the $z < 1$ population. Hence, it is fair to compare these results with those found for the CDFS sample at $0 \leqslant z < 1$ (Table 2). The COSMOS sample nevertheless provides a more numerous sample, giving smaller Poisson errors. The L07 criterion remains the most complete ($\mathcal{C} \sim 80\%$), but also the least reliable ($\mathcal{R} \sim 55\%$–70%), as opposed to D12, which shows the highest reliability levels ($\mathcal{R} \sim 100\%$). KI marginally retrieves a more reliable AGN sample than S05, but comparable completenesses ($\mathcal{C} \sim 60\%$–70% and $\mathcal{R} \sim 90\%$). KIM shows a reliability of ~90%, but is likely the least complete criterion at $z \lesssim 1$.

It is difficult to directly compare in absolute value the results achieved with the CDFS and COSMOS samples, since many characteristics differ between the two surveys. As an example, by applying the COSMOS (IR and X-rays) flux limits to the CDFS sample, the $\mathcal{C}$ and $\mathcal{R}$ values for the different

diagnostics are closer to those of COSMOS. Other issues may contribute to this, such as (1) different photometry extraction methods (ConvPhot by the MUSIC team in CDFS and aperture photometry in COSMOS), (2) different spectral coverage depth and procedures for spectral classification, (3) the different photon indices used for the CDFS and COSMOS samples to convert from count rates to X-ray fluxes, (4) differences in relative sensitivity between soft and hard bands of the *Chandra Space Telescope* (in CDFS) and *XMM-Newton* (in COSMOS), and (5) cosmic variance. We stress, however, that the results on the relative efficiency between the criteria are not contradictory between the two fields.

4.2. IR-excess Sources

Also known as IR bright galaxies, IR-excess (IRxs) sources are believed to be part of an extreme IR population—the Compton-thick (type-2) AGN—frequently missed by optical/X-ray surveys. IRxs sources are always selected to have 24 μm to R-band flux ratio of $f_{24}/f_R > 1000$ (except in Daddi et al. 2007, who select this type of source based on a template fit procedure). However, highly obscured star-forming galaxies may also present such colors (Dey et al. 2008; Fiore et al. 2008; Pope et al. 2008; Georgakakis et al. 2010; Narayanan et al. 2010). It has been shown, nevertheless, that the AGN fraction increases as one restricts IRxs samples to brighter fluxes and/or redder NIR-to-optical colors. Dey et al. (2008) show that at $f_{24\,\mu m} \gtrsim 0.6$, ~50%–80% of the IRxs sample shows power-law SEDs (likely AGN-driven, but see Narayanan et al. 2010), and ~7%–13% have detected X-ray counterparts (a higher fraction than that found for non-IRxs sources). Donley et al. (2010) consider 13 IRxs with $f_{24\,\mu m} \gtrsim 0.7$, which show *Spitzer*-IRS spectra dominated by AGN emission (even though half shows detectable PAH emission), and their X-ray properties hint at heavily obscured (Compton-thick) AGN activity in 80% of the sample. Polletta et al. (2008) considered $f_{24\,\mu m} \gtrsim 1$ IRxs sources, which also presented extremely red NIR-to-optical colors. All selected sources show the 9.7 μm silicate feature in absorption, have extreme MIR luminosities ($L(6\,\mu m) \simeq 10^{46}$ erg s^{-1}), and always require the presence of torus emission to explain their MIR SED. Finally, a simpler color combination was explored to fainter fluxes by Fiore et al. (2008, 2009) and Treister et al. (2009). Through means of X-ray stacking, the two groups showed that >80% of IRxs sources with $(R - K_s)_{\rm Vega} > 4.5$ show evidence for heavily obscured (Compton-thick) AGN activity.

The diagnostics considered below rely on optical-to-IR color cuts, more precisely, $R - K_s$ and $R - [24]$. However, R-band photometry is not available in the MUSIC catalog. We thus convert those colors to equivalent ones using i band ($i - K_s$ and $i - [24]$) considering a power-law spectrum ($f_\nu \propto \nu^\alpha$). We highlight three criteria. Dey et al. (2008, D08) select sources with $S_{24}/S_R > 1000$ and $S_{24} > 300\,\mu$Jy (equivalent to $i - [24] > 7$ and $[24] < 17.5$). Fiore et al. (2008, F08) select $S_{24}/S_R > 1000$ sources with $R - K_s > 4.5$ ($i - [24] > 7$ and $i - K > 2.5$[15]) at $S_{24} > 40\,\mu$Jy ($[24] < 20$). Finally, we also consider the brightest $S_{24}/S_R > 1000$ sources by adopting the flux cut of Polletta et al. (2008, P08), $S_{24} > 1$ mJy (corresponding to $[24] < 16.5$).

These criteria were applied to the MUSIC and COSMOS catalogs and Table 7 details the numbers of the selected sources

---

[15] It should be noted, however, that the $J - K$ color is likely more efficient than $i - K$ in selecting AGN sources (Messias et al. 2010; see also Glikman et al. 2004 for a combination of the two).

Table 7
Selection of IRxs Sources

Region	F08	D08	P08
CDFS			
. . .	77	10	1
L07	72 $(94,15,^{3}_{6})$	9 $(90,41,^{10}_{0})$	1 $(100,100,^{0}_{0})$
S05	29 $(38,8,^{22}_{12})$	5 $(50,27,^{0}_{10})$	1 $(100,100,^{0}_{0})$
D12	18 $(23,6,^{8}_{9})$	5 $(50,27,^{0}_{0})$	1 $(100,100,^{0}_{0})$
KI	40 $(52,10,^{12}_{12})$	7 $(70,34,^{0}_{0})$	1 $(100,100,^{0}_{0})$
KIM	40 $(52,10,^{18}_{8})$	8 $(80,38,^{0}_{0})$	1 $(100,100,^{0}_{0})$
COSMOS			
. . .	991	256	51
L07	909 $(92,4,^{6}_{12})$	244 $(95,9,^{1}_{4})$	47 $(92,19,^{2}_{6})$
S05	381 $(38,2,^{15}_{11})$	138 $(54,6,^{7}_{4})$	39 $(76,16,^{2}_{6})$
D12	202 $(20,2,^{7}_{4})$	128 $(50,5,^{4}_{3})$	41 $(80,17,^{4}_{0})$
KI	493 $(50,3,^{16}_{12})$	179 $(70,7,^{8}_{3})$	46 $(90,18,^{4}_{2})$
KIM	606 $(61,3,^{17}_{18})$	212 $(83,8,^{6}_{9})$	50 $(98,20,^{0}_{0})$

Notes. Number of selected IRxs sources. The numbers in parentheses give the equivalent fractions, the Poisson error, and the photometric upper and lower error bars.

by each of the IR color criteria. In spite of the much smaller sample size in CDFS, the results agree remarkably well between the two surveys. In COSMOS, all criteria appear to select most of the brightest objects (P08) in a comparable way (within the error bars), as expected (Donley et al. 2008; Eckart et al. 2010). Regarding the fainter sources, L07 is the most complete, followed by KIM and KI, while S05 and D12 select the fewest IRxs sources.

4.3. SDSS QSOs

QSOs present in the Sloan Digital Sky Survey Quasar Catalogue Data Release 7 (SDSS-DR7; Schneider et al. 2010) were cross-matched ($2''$ radius) with the *Spitzer* IR catalogs from the COSMOS (S-COSMOS), Lockman Hole, ELAIS-N1, and ELAIS-N2 (SWIRE; Lonsdale et al. 2003) fields using GATOR[16] at IRSA-NASA/IPAC. The final sample is composed of 293 QSOs. K_s-band photometry comes from 2MASS (for 21% of the sample; Skrutskie et al. 2006), UKIDSS-DXS DR8[17] (29%; Lawrence et al. 2007), and COSMOS (23%; Ilbert et al. 2009). Overall, there are 186 QSOs with reliable photometry in all IRAC channels. Of these, 140 also have MIPS$_{24\,\mu m}$ photometry, and 142 have K_s-band photometry. We find 107 with full K_s–IRAC–MIPS$_{24\,\mu m}$ coverage. To enhance the high-z regime sampling, we further include 13 SDSS-DR3 QSOs at $z \sim 6$ (Jiang et al. 2006). Of these, 12 are detected in all IRAC and MIPS$_{24\,\mu m}$ channels, while only five have 2MASS K_s-band data.

Figure 9 shows the location of the QSO sample in the KI, IM (Section 3.2), L07, and S05 color–color spaces. Only sources with reliable photometry in the displayed bands are shown. While L07, S05, and KI select most of the displayed sample (>90%), D12 and KIM select a smaller, yet large, portion of it, respectively, 84% and 65%. For $z > 5$ QSOs, the IM completeness drops to 36%, in agreement with Figure 5, where QSO templates start to move out of the KIM region at $z \sim 4$–5.

---

[16] http://irsa.ipac.caltech.edu/applications/Gator/
[17] UKIDSS uses the UKIRT Wide Field Camera (WFCAM; Casali et al. 2007) and a photometric system described in Hewett et al. (2006). The pipeline processing and science archive are described in Irwin (2008) and Hambly et al. (2008). We have used data from the 8th data release.
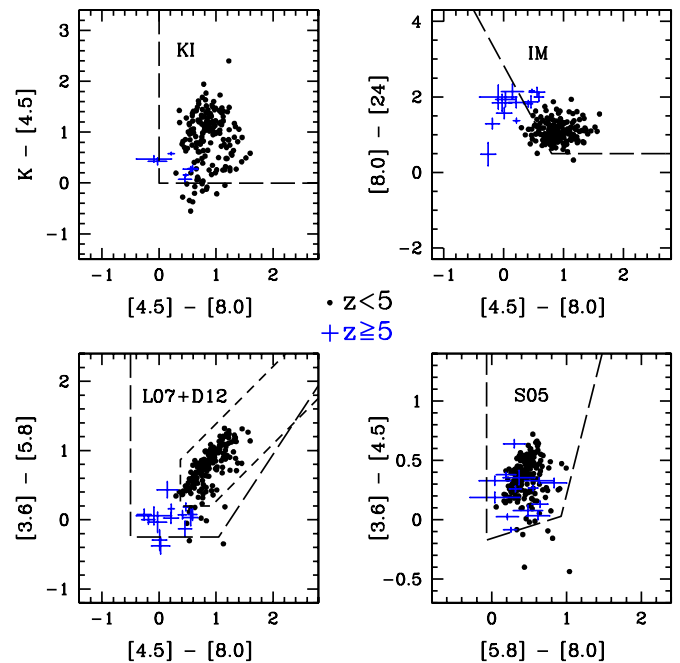
Figure 9. SDSS-DR7 QSOs found in the SWIRE and COSMOS fields together with the Jiang et al. (2006) sample displayed in KI (top left), IM (top right), L07 and D12 (bottom left), and S05 (bottom right) color–color spaces. Black dots represent $z < 5$ (with small average photometric errors), and blue dots (with error bars) otherwise.
(A color version of this figure is available in the online journal.)

This is likely a result of blue rest-frame optical SEDs, which most IRAC bands probe at these redshifts, low metallicity (consequently less dust) in these high-redshift sources, and strong Hα emission. While blue rest-frame optical SEDs or strong Hα emission imply more objects in the blue side of $[4.5] - [8.0]$, low metallicity results in some objects with bluer $[8.0] - [24]$ colors. Note that S05 and D12 retrieve opposite efficiencies in selecting $z > 5$ QSOs, where S05 selects all and D12 selects none.

We note, however, that if there is a prior indication for such high redshifts ($z > 3$ based on spectroscopy or, e.g., on the LBG technique), then the $[8.0]-[24]$ color can be used by itself and much more efficiently for the identification of AGNs (cf. Figure 6). For $z > 5$ QSOs, all but one show $[8.0] - [24] > 1$. The few QSOs with blue $K_s - [4.5]$ (top left panel) colors are explained in light of the discussion in Section 3.1: these are potentially AGNs with smaller optical-to-IR flux ratios and/or sources possessing strong line emission.

The high completeness levels achieved with this optical-selected sample show the eclectic selection of IR criteria. However, optically selected AGNs are not the main targets of IR AGN diagnostics, as, by definition, optical surveys *do* detect them. The most interesting use of these criteria is to recover sources undetected at X-ray and optical wavelengths. Sections 4.2 (above) and 4.4 (below) are, in this respect, much more representative of the usefulness of IR AGN diagnostics.
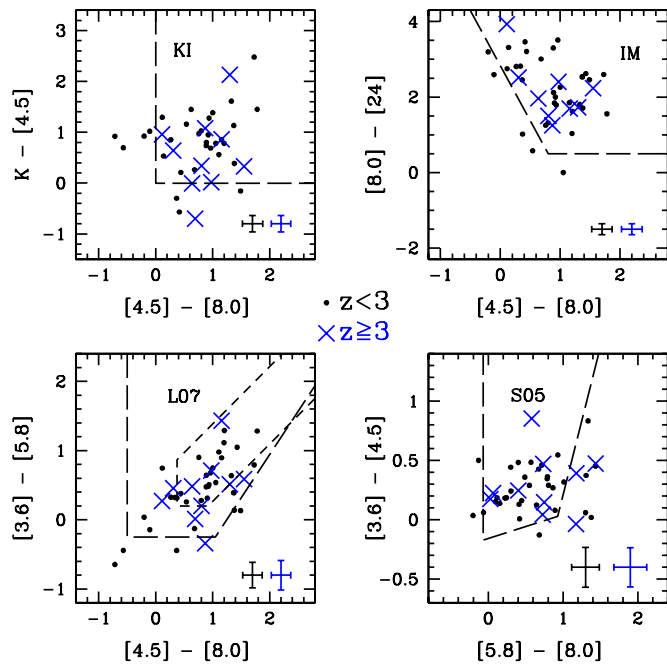
4.4. High-redshift Radio Galaxies

To test yet another AGN population, we now consider HzRGs. These are among the most luminous sources in the universe and are believed to host powerful AGNs. We use the sample of 71 HzRGs from Seymour et al. (2007). These are all at $z > 1$, a redshift range where no normal galaxy is believed to

Figure 10. HzRG ($z > 1$) sample from Seymour et al. (2007) displayed in the same color–color spaces as in Figure 9. Note the objects at $2 < [8.0] − [24] < 4$ which are even redder than QSOs (Figure 9). Dots show the $z < 3$ population, crosses show the population at $z \geqslant 3$. The average photometric errors of this sample are shown on the bottom right of each panel for the $z < 3$ (left error bars) and $z \geqslant 3$ (right) samples.

(A color version of this figure is available in the online journal.)

Figure 11. SMG sample from Chapman et al. (2005) displayed in the same color–color spaces as in Figure 9. Only sources detected in the referred bands in each panel are displayed. The average photometric errors are shown on the bottom right of each panel. The data point intensity shows the AGN fraction at observed $8\,\mu$m (intensity bar in the center). Sources with AGN contribution upper limits are shown as crosses.

contaminate the AGN IM region proposed in Section 3.2. This is a classic example—such as that of LBGs or spectroscopically confirmed galaxies at $z > 1$—for the direct application of the IM boundaries. Having this, the $K_s − [4.5] > 0$ color cut is not required to disentangle AGN/non-AGN-dominated sources at $z < 1$ (see Section 3.1), meaning that one may consider $[4.5] − [8.0]$ and $[8.0] − [24]$ colors alone to determine whether AGN or stellar emission dominates the IR spectral regime.

Figure 10 shows the location of 62 HzRGs in the IM color–color diagram (top right panel). Note the difference to SDSS QSOs (Figure 9), where HzRGs show predominantly redder $[8.0] − [24]$ colors. The AGN region correctly selects as AGN 88% (37 sources) of the sample with adequate photometry (42 sources detected at 4.5, 8.0, and 24 μm). If no redshift estimate was available, however, one would need the $K_s − [4.5] > 0$ color cut to apply the IM AGN criterion, i.e., the KIM criterion. The application of KIM would result in a 78% completeness level (28 out of 36 sources). The remaining panels show that L07 selects 86% (38 out of 44 sources), D12 selects 27% (12 out of 44 sources), S05 selects 73% (32 out of 44 sources), and KI selects 78% (32 out of 41 sources).

Again we emphasize that much of the improvement of KI/KIM over the commonly used L07 and S05 diagnostics is in terms of reliability, an indicator which is not being evaluated with this sample nor those in Sections 4.2 and 4.3.

4.5. Submillimeter Galaxies

In Hainline et al. (2011), one can find estimates for the non-stellar contribution (shown in that work to be related to AGN activity) to the IR SED of SMGs, showing that significant AGN emission is present even at $1.6\,\mu$m ($\sim$50%–60% of the sample with an estimate shows AGN contributions of

$\gtrsim$20%–10% at these wavelengths). The estimates for the non-stellar contribution were obtained photometrically by fitting the SMG SEDs with a combination of pure star-forming models and power-law spectra ($f \propto \nu^\alpha$, with $\alpha = −2$ or $−3$). These non-stellar contribution estimates depend on whether one considers a constant SF history or an initial instant burst followed by passive evolution. These assumptions provide two extreme scenarios, and here we adopt the average between the two. The sample is that from Chapman et al. (2005), found to be at $0.1 \lesssim z_{\mathrm{spec}} \lesssim 3.4$ ($\sim$85% of the sample is at $z_{\mathrm{spec}} > 1$). The K-band photometry is presented in Smail et al. (2004), while the IRAC and MIPS photometry is presented in Hainline et al. (2009).

Figure 11 shows the distribution of SMGs in different color–color spaces. The intensity of each data point relates to the AGN contribution at observed $8\,\mu$m (the darker it is, the higher is the AGN contribution). Specifically in the IM plot (upper right panel), even though there are two sources with an estimated 0% contribution from AGNs inside the selection region, all but one (with 25%) of the remainder (19 sources) have $\geqslant$50% of AGN contribution. Overall, the IM-selected sample shows an average of $62^{+3}_{-5}\%$[18] of AGN contribution at observed $8\,\mu$m. L07, S05, D12, and KI show,[19] respectively, averages of $55^{+2}_{-3}\%$, $66^{+2}_{-4}\%$, $75^{+3}_{-7}\%$, and $60^{+3}_{-5}\%$. Although all criteria select at least one SMG with an estimated 0% contribution from AGNs, the average AGN contribution is always $\geqslant$55%. This means that for many SMGs, although the AGN does not dominate the IR emission, the AGN contributes significantly to the IR SED of the galaxy. The same is expected for IR-selected AGNs; this is

---

[18] The errors only consider the propagated errors associated with each individual estimate used for averaging.

[19] Separately considering sources detected in bands involved in each criteria, hence subject to selection effects. For instance, 49 SMGs are detected in all four IRAC channels (used for L07, S05, and D12 statistics), while 34 are detected in K_s band, 4.5 μm and 8.0 μm (used for KI statistics).
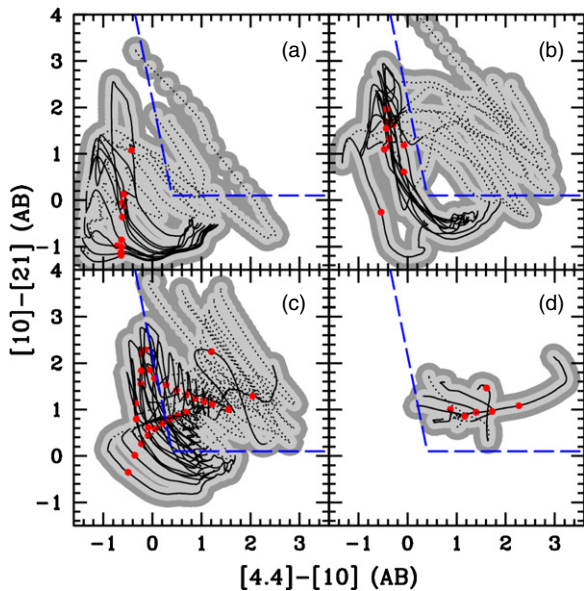
Figure 12. Alternative color–color space with *JWST* bands which might improve the AGN selection at $0 < z < 7$. Symbols and panel definitions are the same as in Figure 2. The light-/dark-gray error circles in the tracks result from larger color gradients between redshift steps ($\Delta z = 0.01$ each). These "circles" correspond to the error ellipse of each redshift point in the color tracks.

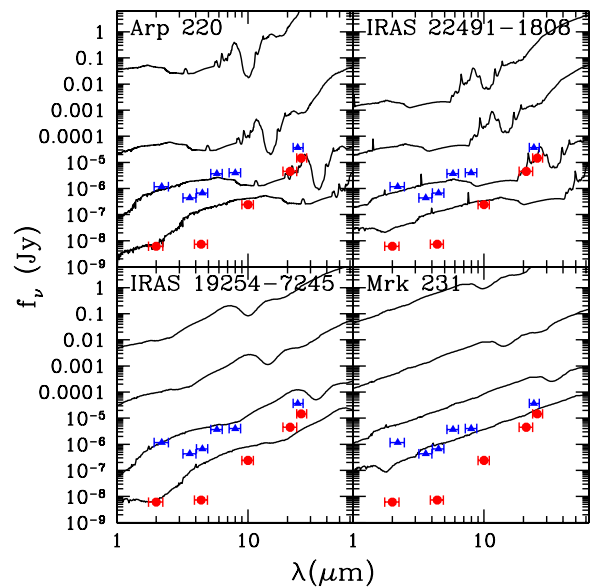(A color version of this figure is available in the online journal.)

because, although we see selected sources where the AGN does not dominate at IR wavelengths, the AGN is present and active, contributing enough for the source to be selected as an IR AGN.

5. IMPLICATIONS FOR *JWST* SURVEYS

The start of scientific observations by *JWST*, the successor of *Spitzer* at mid-IR wavelengths, is expected in 2018. It will be a 6.5 m space telescope which will operate from 0.6 to 27 μm. As highlighted in this and previous work, this spectral regime has great potential for separating AGNs from normal (non-AGN) galaxies.

The sensitivity will, of course, be better than ever before, and the high-z universe will be probed with unprecedented detail. Many galaxies will be studied with MIR spectroscopy, and signs of AGN activity will be naturally found that way (e.g., Laurent et al. 2000; Armus et al. 2007; Veilleux et al. 2009; Fu et al. 2010). When dealing with large surveys, however, with thousands of sources and many close to the detection limit, AGN selection will have to rely on photometric diagnostics such as the KI/KIM criteria presented here. By selecting AGN candidates over a broad range of redshifts, $0 < z < 7$, the KIM criterion will enable the study of AGN phenomena to the earliest epochs.

While the KI/KIM criteria can already be applied to current data from *Spitzer*, potentially more efficient MIR criteria will be possible with the large wavelength coverage of the *JWST*. Using planned *JWST* filter response curves,[20] we suggest a possible and promising color–color space alternative to that proposed in Section 3.2, using the MIRI 10 μm and 21 μm filters instead of the IRAC 8.0 μm and MIPS 24 μm bands, and the NirCAM 4.4 μm instead of IRAC 4.5 μm (note that these are bands close to those used in *Wide-field IR Survey Explorer*, *WISE*; see also

---

[20] Provided online at http://www.stsci.edu/jwst/instruments/nircam/instrumentdesign/filters/index_html
http://www.stsci.edu/jwst/instruments/miri/instrumentdesign/miri_glance.html.

Figure 13. SED flux evolution with redshift for two SF-dominated systems (Arp220 and IRAS 22491−1908, upper panels), and two AGN-dominated systems (IRAS 19254−7245 and Mrk231, lower panels). The redshift steps are $z = z_0$, 0.5, 2.5, 7. The blue dots indicate the K_s–IRAC–MIPS$_{24\,\mu m}$ CDFS 10σ total flux level (based on Table 1 of Wuyts et al. 2008), red dots give the 10σ level (at equivalent CDFS integration times) of the *JWST* filters: 2.0 μm, 4.4 μm, 10 μm, 21 μm, and 25 μm. At longer wavelengths, the gap between *Spitzer* and *JWST* sensitivities is smaller due to the warmer telescope thermal background of *JWST*.

(A color version of this figure is available in the online journal.)
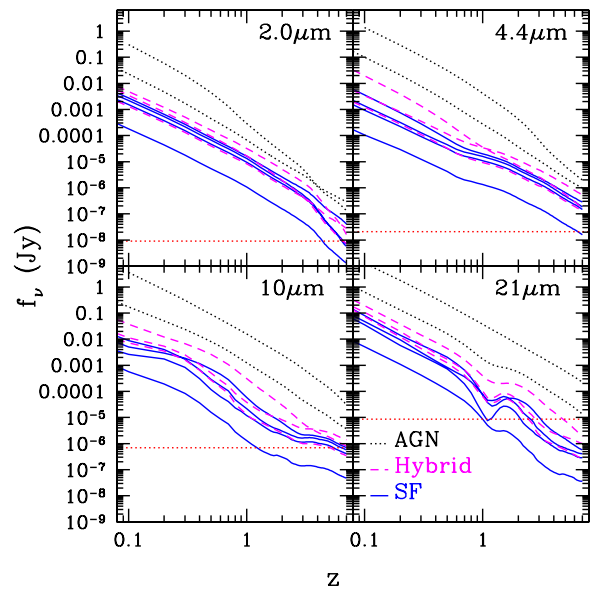
Figure 14. Flux evolution with redshift for starbursts (blue solid line), hybrids (magenta dashed line), and AGNs (black dotted line) in four *JWST* filters. Red dotted horizontal lines mark the 10σ level (10,000 s integration) of each filter.

(A color version of this figure is available in the online journal.)

Assef et al. 2010; Stern et al. 2012). The selection conditions are as follows:

$$[10] - [21] > -5.2 \times ([4.4] - [10]) + 2.2$$

and

$$[10] - [21] > 0.1.$$

In Figure 12, the four panels show that the [4.4]−[10] versus [10]−[21] color–color space seems to present a better selection of the AGN/hybrid model tracks. The AGN model tracks are better delineated by the selection boundaries (recovering the $z \gtrsim$ 4–5 QSO missed by KIM) and, as a bonus, the 21 μm filter is over three times more sensitive than the planed MIRI 25 μm filter (equivalent to the MIPS 24 μm filter), increasing the probability of a detection needed for an AGN classification. This is shown in Figures 13 and 14, where AGN-dominated sources are detected up to the highest redshift considered in this work ($z \sim 7$).

Finally, the improved resolution of *JWST* will allow the study of the nuclear region alone up to higher redshifts. This, of course, allows the identification of lower luminosity AGNs (e.g., Hönig et al. 2010; Asmus et al. 2011), thus overcoming the difficulty in selecting such systems in the IR.

6. CONCLUSIONS

Based on semi-empirical galaxy SED templates, we have developed physically motivated IR color criteria for the selection of a wide variety of AGNs in a large redshift range ($0 < z < 7$). As well as the application to existing data (e.g., the recently available *WISE* data[21] at 3.4, 4.6, 12, and 22 μm; Wright et al. 2010), these criteria are particularly relevant for the *JWST*, given the wide MIR spectral range considered. We thus propose new AGN IR diagnostics. The $K_s - [4.5]$ color is ideal for the $z < 1$ universe (Section 3.1); KI is a reliable alternative to the IRAC-based diagnostics at $z \lesssim 2.5$ (based on Poisson errors alone, Sections 3.1 and 4.1); and KIM (Section 3.2), a four-band (K_s, 4.5, 8.0, and 24 μm), three-color ($K_s-[4.5]$, $[4.5]-[8.0]$, and $[8.0]-[24]$) criterion is proposed as a new "wedge" criterion to select AGN hosts over the full $0 < z < 7$ range, based on template color tracks alone (the current control samples prevent any conclusion at $z \gtrsim 2.5$ due to small sample statistics).

The *absolute* efficiency of IR AGN criteria is, at this stage, impossible to obtain as the control (X-ray- and optical-selected) samples used here are themselves incomplete; hence, results should be treated with care. For instance, KI achieves reliabilities of $\sim$50% in CDFS ($\sim$90% in COSMOS) and KIM shows reliabilities of $\sim$60%–80% ($\sim$90%). These should be considered lower limits, because X-ray and spectroscopic data may not have been deep enough to reveal AGN features (Section 4), and we show that the selected sources with SF-dominated SEDs are still likely to host an active AGN.

Nevertheless, in the coming years, these criteria should be improved as a result of the rich variety of filters to be incorporated in the instruments on board the upcoming *JWST* (Section 5). The ability to track AGN activity since the end of the reionization epoch will hold great advantages for the study of galaxy–AGN co-evolution.

APPENDIX

It has been pointed out that the estimate of column densities (N_H) based on soft-to-hard X-ray flux ratios overestimates the type-2 (obscured) object fraction with increasing redshift (Ueda et al. 2003; Akylas et al. 2006; Donley et al. 2012). The fact that we consider soft-to-full or hard-to-full band ratios does not change the scenario. This bias effect happens due to a harder spectral range being probed at higher redshifts by the observed 0.5–8/10 keV spectral window plus the error associated with the flux measurement. Figure 15(a) shows the soft-to-full ratio variation depending on redshift and N_H. One can see that, with increasing redshifts, for the smallest N_H values the associated flux ratios become problematically degenerate.[22] Would there be perfect precision and accuracy in the flux measurements, this would hold no problem; however, there is a flux error which scatters the real values producing the observational bias. Figure 15(b) shows the observed values from the CDFS and COSMOS samples for reference.

Figure 16(a) shows the overall bias toward type-2 objects over type-1 objects depending on redshift and flux ratio error (in percent). In order to produce this figure, we have considered an initial 50%/50% fraction of type-1/type-2 objects and a Gaussian probability density distribution (PDD) centered at flux ratios corresponding to $19 < \log(N_H[\mathrm{cm}^{-2}]) < 25$ and with a $\sigma = 5\%, 10\%, 20\%, 30\%$ of the flux ratio. The Gaussian PDD gives the probability for the output (observed) classification to be *unobscured* ($\log(N_H[\mathrm{cm}^{-2}]) \leqslant 22$) or *obscured* ($\log(N_H[\mathrm{cm}^{-2}]) > 22$), consequently providing the overall output bias shown in Figure 16(a). In this figure, the bias is calculated as the ratio between the output (observed) type-2/type-1 ratio and the input (intrinsic) type-2/type-1 ratio. Note the trends maximize at $\sim$2. If we had instead restricted this exercise to the $20 < \log(N_H[\mathrm{cm}^{-2}]) < 24$ range (considered in Donley et al. 2012), the maximum value would be at $\sim$1.8. This is the bias found by Donley et al. (2012) at $z \sim 3$. This means, for the $z \sim 3$ *XMM* sources used in that work, the flux ratios are affected on average by a $\sim$30% error.

The Gaussian PDD also provides the average overestimate associated with a given intrinsic N_H value depending on flux ratio error and redshift. This is shown in Figure 16(b) for a 20% flux ratio error. These trends allow us to attempt the correction of the referred bias, where the observed N_H value (y-axis in Figure 16(b)) corresponds to an intrinsically smaller N_H value (x-axis) for a given flux ratio error at the source's redshift. The flux ratios used to estimate N_H in this work are all based on measurements with errors less than a third of the fluxes, a propagated flux ratio error of $<47\%$ (the average accepted flux ratio error was $\sim$19%). Even though individually the corrected value *should not* be regarded as the best estimate, this average correction applied to the overall population will diminish the bias. The number of type-1 objects which would be classified as type-2 if no correction was applied is small: 14 in CDFS and 9 in COSMOS. Most of these (19 objects) are at $z \gtrsim 3$.

---

[22] At $z \sim 0$, there is also a degeneracy at $\log(N_H[\mathrm{cm}^{-2}]) = 23$–25, but it does not represent a problem because the constraint considered to distinguish type-1 from type-2 objects is $\log(N_H[\mathrm{cm}^{-2}]) = 22$.
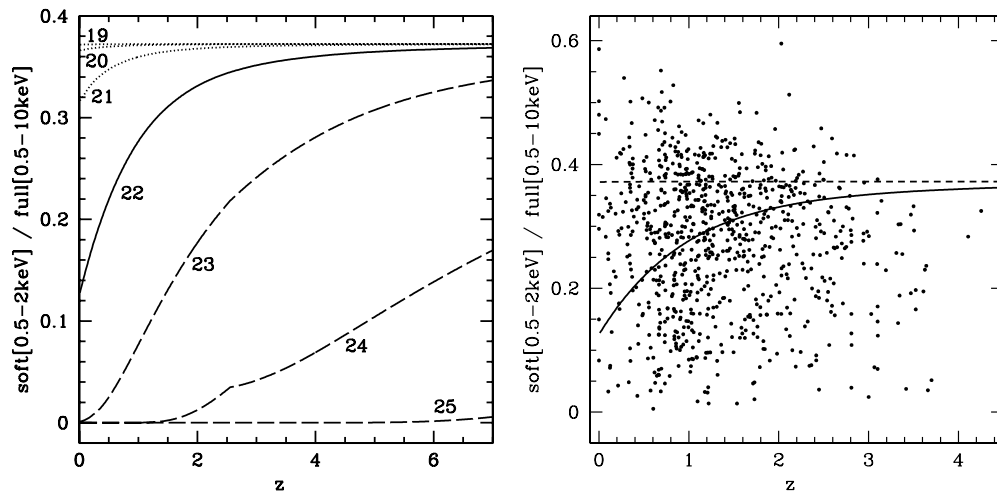
Figure 15. Left-hand panel shows the dependency of the flux ratio on column density ($N_{\rm H}$) and redshift. The numbers refer to the $\log(N_{\rm H}[{\rm cm}^{-2}])$ value corresponding to each line. The reference level $\log(N_{\rm H}[{\rm cm}^{-2}]) = 22$ is shown as the solid line. The right-hand panel shows the observed flux ratios for the CDFS and COSMOS samples. The $\log(N_{\rm H}[{\rm cm}^{-2}]) = 22$ value is again shown as a solid line for reference, as well as the $\log(N_{\rm H}[{\rm cm}^{-2}]) = 19$ value, above which we have considered $\log(N_{\rm H}[{\rm cm}^{-2}]) = 0$ and the observed photon index to estimate X-ray luminosities.
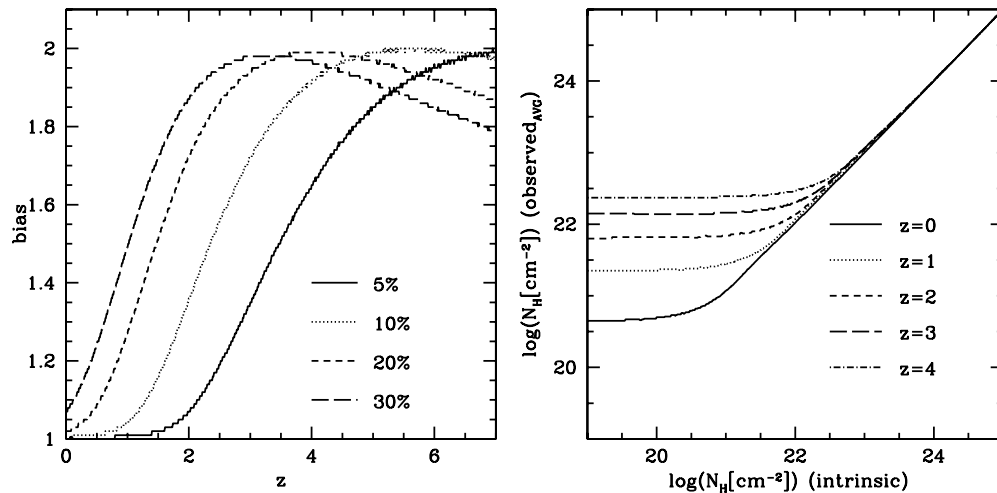
Figure 16. Panel (a) shows the evolution of the bias toward type-2 objects with redshift for different levels of error in the flux ratio estimate. Panel (b) shows, for a 20% error level in the flux ratio estimate, the average overestimate depending on column density ($N_{\rm H}$) and redshift.

REFERENCES

Adelberger, K. L., Steidel, C. C., Shapley, A. E., et al. 2004, ApJ, 607, 226
Afonso, J., Mobasher, B., Chan, B., & Cram, L. 2001, ApJ, 559, 101
Afonso, J., Mobasher, B., Koekemoer, A., Norris, R. P., & Cram, L. 2006, AJ, 131, 1216
Akylas, A., Georgantopoulos, I., Georgakakis, A., Kitsionas, S., & Hatziminaoglou, E. 2006, A&A, 459, 693
Alexander, D. M., Bauer, F. E., Chapman, S. C., et al. 2005, ApJ, 632, 736
Alonso-Herrero, A., Pérez-González, P. G., Alexander, D. M., et al. 2006, ApJ, 640, 167
Armus, L., Charmandaris, V., Bernard-Salas, J., et al. 2007, ApJ, 656, 148
Asmus, D., Gandhi, P., Smette, A., Hönig, S. F., & Duschl, W. J. 2011, A&A, 536, 36
Assef, R. J., Kochanek, C. S., Ashby, M. L. N., et al. 2011, ApJ, 728, 56
Assef, R. J., Kochanek, C. S., Brodwin, M., et al. 2010, ApJ, 713, 970
Barmby, P., Alonso-Herrero, A., Donley, J. L., et al. 2006, ApJ, 642, 126
Bongiorno, A., Mignoli, M., Zamorani, G., et al. 2010, A&A, 510, 56
Bower, R. G., Benson, A. J., Malbon, R., et al. 2006, MNRAS, 370, 645
Brand, K., Dey, A., Weedman, D., et al. 2006, ApJ, 644, 143
Brusa, M., Civano, F., Comastri, A., et al. 2010, ApJ, 716, 348
Calzetti, D., Kennicutt, R. C., Engelbracht, C. W., et al. 2007, ApJ, 666, 870
Cappelluti, N., Brusa, M., Hasinger, G., et al. 2009, A&A, 497, 635
Cardamone, C. N., Urry, C. M., Damen, M., et al. 2008, ApJ, 680, 130
Casali, M., Adamson, A., Alves de Oliveira, C., et al. 2007, A&A, 467, 777

Chambers, K. C., Miley, G. K., van Breugel, W. J. M., & Huang, J.-S. 1996, ApJS, 106, 215
Chapman, S. C., Blain, A. W., Smail, I., & Ivison, R. J. 2005, ApJ, 622, 772
Comastri, A., Fiore, F., Vignali, C., et al. 2001, MNRAS, 327, 781
Croton, D. J., Springel, V., White, S. D. M., et al. 2006, MNRAS, 365, 11
Daddi, E., Dickinson, M., Morrison, G., et al. 2007, ApJ, 670, 156
Dey, A., Soifer, B. T., Desai, V., et al. 2008, ApJ, 708, 943
de Grijp, M. H. K., Miley, G. K., Lub, J., & de Jong, T. 1985, Nature, 314, 240
Donley, J. L., Koekemoer, A. M., Brusa, M., et al. 2012, ApJ, 748, 142
Donley, J. L., Rieke, G. H., Alexander, D. M., Egami, E., & Pérez-González, P. G. 2010, ApJ, 719, 1393
Donley, J. L., Rieke, G. H., Pérez-González, P. G., & Barro, G. 2008, ApJ, 687, 111
Donley, J. L., Rieke, G. H., Pérez-González, P. G., Rigby, J. R., & Alonso-Herrero, A. 2007, ApJ, 660, 167
Draper, A. R., & Ballantyne, D. R. 2009, ApJ, 707, 778
Eckart, M., McGreer, I. D., Stern, D., Harrison, F. A., & Helfand, D. J. 2010, ApJ, 708, 584
Eckart, M. E., Stern, D., Helfand, D. J., et al. 2006, ApJS, 165, 19
Edelson, R., & Malkan, M. 2012, ApJ, 751, 52
Elbaz, D., Dickinson, M., Hwang, H. S., et al. 2011, A&A, 533, A119
Elbaz, D., Flores, H., Chanial, P., et al. 2002, A&A, 381, L1
Elvis, M., Wilkes, B. J., McDowell, J. C., et al. 1994, ApJS, 95, 1
Engelbracht, C. W., Rieke, G. H., Gordon, K. D., et al. 2008, ApJ, 678, 804
Fadda, D., Yan, L., Lagache, G., et al. 2010, ApJ, 719, 425
Farrah, D., Bernard-Salas, J., Spoon, H. W. W., et al. 2007, ApJ, 667, 149

Fazio, G. G., Hora, J. L., Allen, L. E., et al. 2004, ApJS, 154, 1
Fiore, F., Grazian, A., Santini, P., et al. 2008, ApJ, 672, 94
Fiore, F., Puccetti, S., Brusa, M., et al. 2009, ApJ, 693, 447
Fu, H., Yan, L., Scoville, N. Z., et al. 2010, ApJ, 722, 653
Garn, T., Sobral, D., Best, P. N., et al. 2010, MNRAS, 402, 2017
Georgakakis, A., Rowan-Robinson, M., Nandra, K., et al. 2010, MNRAS, 406, 420
Giacconi, R., Rosati, P., Tozzi, P., et al. 2001, ApJ, 551, 624
Gilli, R. 2004, Adv. Space Res., 34, 2470
Glikman, E., Gregg, M. D., Lacy, M., et al. 2004, ApJ, 607, 60
Granato, G. L., De Zotti, G., Silva, L., Bressan, A., & Danese, L. 2004, ApJ, 600, 580
Grazian, A., Fontana, A., de Santis, C., et al. 2006, A&A, 449, 951
Hainline, L. J., Blain, A. W., Smail, I., et al. 2009, ApJ, 699, 1610
Hainline, L. J., Blain, A. W., Smail, I., et al. 2011, ApJ, 740, 96
Hambly, N. C., Collins, R. S., Cross, N. J. G., et al. 2008, MNRAS, 384, 637
Hatziminaoglou, E., Pérez-Fournon, I., Polletta, M., et al. 2005, AJ, 129, 1198
Henriques, B., Maraston, C., Monaco, P., et al. 2011, MNRAS, 415, 3571
Hewett, P. C., Warren, S. J., Leggett, S. K., & Hodgkin, S. T. 2006, MNRAS, 367, 454
Ho, L. C., Terashima, Y., & Ulvestad, J. S. 2003, ApJ, 589, 783
Hönig, S. F., Kishimoto, M., Gandhi, P., et al. 2010, A&A, 515, A23
Hopkins, P. F., Hernquist, L., Cox, T. J., et al. 2006, ApJS, 163, 1
Hopkins, P. F., Hernquist, L., Martini, P., et al. 2005, ApJ, 625, L71
Hu, E. M., & Ridgway, S. E. 1994, AJ, 107, 1303
Hunt, L. K., Thuan, T. X., Izotov, Y. I., & Sauvage, M. 2010, ApJ, 712, 164
Ilbert, O., Capak, P., Salvato, M., et al. 2009, ApJ, 690, 1236
Irwin, M. J. 2008, in The 2007 ESO Instrument Calibration Workshop, ed. A. Kaufer & F. Kerber (Berlin: Springer), 541
Ivezić, Ž., Menou, K., Knapp, G. R., et al. 2002, AJ, 124, 2364
Ivison, R. J., Greve, T. R., Serjeant, S., et al. 2004, ApJS, 154, 124
Jiang, L., Fan, X., Hines, D. C., et al. 2006, AJ, 132, 2127
Lacy, M., Petric, A. O., Sajina, A., et al. 2007, AJ, 133, 186
Lacy, M., Storrie-Lombardi, L. J., Sajina, A., et al. 2004, ApJS, 154, 166
Laor, A. 1999, Phys. Rep., 311, 451
Laurent, O., Mirabel, I. F., Charmandaris, V., et al. 2000, A&A, 359, 887
Lawrence, A., Warren, S. J., Almaini, O., et al. 2007, MNRAS, 379, 1599
Le Floc'h, E., Aussel, H., Ilbert, O., et al. 2009, ApJ, 703, 222
Loewenstein, M., Mushotzky, R. F., Angelini, L., Arnaud, K. A., & Quataert, E. 2001, ApJ, 555, L21
Lonsdale, C. J., Smith, H. E., Rowan-Robinson, M., et al. 2003, PASP, 115, 897
Luo, B., Bauer, F. E., Brandt, W. N., et al. 2008, ApJS, 179, 19
Luo, B., Brandt, W. N., Xue, Y. Q., et al. 2010, ApJS, 187, 560
Maiolino, R., Comastri, A., Gilli, R., et al. 2003, MNRAS, 344, 59
Maraston, C. 2005, MNRAS, 362, 799
Martínez-Sansigre, A., Rawlings, S., Lacy, M., et al. 2005, Nature, 436, 666
McCracken, H. J., Capak, P., Salvato, M., et al. 2010, ApJ, 708, 202
Melia, F., & Falcke, H. 2001, ARA&A, 39, 309
Messias, H., Afonso, J., Hopkins, A., et al. 2010, ApJ, 719, 790
Miley, G. K., Neugebauer, G., & Soifer, B. T. 1985, ApJ, 293, L11
Morganti, R., Holt, J., Tadhunter, C., et al. 2011, A&A, 535, 97
Narayanan, D., Dey, A., Hayward, C. C., et al. 2010, MNRAS, 407, 1701
Neugebauer, G., Habing, H. J., van Duinen, R., et al. 1984, ApJ, 278, L1
Neugebauer, G., Oke, J. B., Becklin, E. E., & Matthews, K. 1979, ApJ, 230, 79
Norris, R. P., Afonso, J., Cava, A., et al. 2011, ApJ, 736, 55
Papovich, C., Moustakas, L. A., Dickinson, M., et al. 2006, ApJ, 640, 92

Papovich, C., Rudnick, G., Le Floc'h, E., et al. 2007, ApJ, 668, 45
Patten, B. M., Stauffer, J. R., Burrows, A., et al. 2006, ApJ, 651, 502
Petric, A. O., Armus, L., Howell, J., et al. 2011, ApJ, 730, 28
Pier, E. A., & Krolik, J. H. 1992, ApJ, 401, 99
Polletta, M., Tajer, M., Maraschi, L., et al. 2007, ApJ, 663, 81
Polletta, M., Weedman, D., Hönig, S., et al. 2008, ApJ, 675, 960
Polletta, M., Wilkes, B. J., Siana, B., et al. 2006, ApJ, 642, 673
Pope, A., Chary, R.-R., Alexander, D. M., et al. 2008, ApJ, 675, 1171
Pozzi, F., Vignali, C., Gruppioni, C., et al. 2012, MNRAS, 3072 (arXiv:1204.1152)
Richards, G. T., Deo, R. P., Lacy, M., et al. 2009, AJ, 137, 3884
Richards, G. T., Fan, X., Newberg, H. J., et al. 2002, AJ, 123, 2945
Rieke, G. H., Alonso-Herrero, A., Weiner, B. J., et al. 2009, ApJ, 692, 556
Rigby, J. R., Marcillac, D., Egami, E., et al. 2008, ApJ, 675, 262
Roche, N. D., Dunlop, J., & Almaini, O. 2003, MNRAS, 346, 803
Sajina, A., Lacy, M., & Scott, D. 2005, ApJ, 621, 256
Salvato, M., Hasinger, G., Ilbert, O., et al. 2009, ApJ, 690, 1250
Salvato, M., Ilbert, O., Hasinger, G., et al. 2011, ApJ, 742, 61
Sanders, D. B. 1999, in IAU Symp. 194, Active Galactic Nuclei and Related Phenomena, ed. Y. Terzian, E. Khachikian, & D. Weedman (San Francisco, CA: ASP), 25
Sanders, D. B., Phinney, E. S., Neugebauer, G., Soifer, B. T., & Matthews, K. 1989, ApJ, 347, 29
Sanders, D. B., Salvato, M., Aussel, H., et al. 2007, ApJS, 172, 8
Sani, E., & Nardini, E. 2012, Adv. Astron., 2012, 783451
Santini, P., Fontana, A., Grazian, A., et al. 2009, A&A, 504, 751
Schneider, D. P., Richards, G. T., Hall, P. B., et al. 2010, AJ, 139, 2360
Scoville, N., Aussel, H., Brusa, M., et al. 2007, ApJS, 172, 1
Seymour, N., Stern, D., De Breuck, C., et al. 2007, ApJS, 171, 353
Simpson, C., Martínez-Sansigre, A., Rawlings, S., et al. 2006, MNRAS, 372, 741
Skrutskie, M. F., Cutri, R. M., Stiening, R., et al. 2006, AJ, 131, 1163
Smail, I., Chapman, S. C., Blain, A. W., & Ivison, R. J. 2004, ApJ, 616, 71
Somerville, R. S., Hopkins, P. F., Cox, T. J., Robertson, B. E., & Hernquist, L. 2008, MNRAS, 391, 481
Springel, V., Di Matteo, T., & Hernquist, L. 2005, MNRAS, 361, 776
Steidel, C. C., Adelberger, K. L., Shapley, A. E., et al. 2003, ApJ, 592, 728
Steidel, C. C., Shapley, A. E., Pettini, M., et al. 2004, ApJ, 604, 534
Stern, D., Assef, R. J., Benford, D. J., et al. 2012, arXiv:1205.0811
Stern, D., Eisenhardt, P., Gorjian, V., et al. 2005, ApJ, 631, 163
Szokoly, G. P., Bergeron, J., Hasinger, G., et al. 2004, ApJS, 155, 271
Tielens, A. G. G. M., Miley, G. K., & Willis, A. G. 1979, A&AS, 35, 153
Tozzi, P., Gilli, R., Mainieri, V., et al. 2006, A&A, 451, 457
Treister, E., Cardamone, C. N., Schawinski, K., et al. 2009, ApJ, 706, 535
Treister, E., & Urry, C. M. 2005, ApJ, 630, 115
Treister, E., & Urry, C. M. 2012, Adv. Astron., 2012, 516193
Treister, E., Urry, C. M., Van Duyne, J., et al. 2006, ApJ, 640, 603
Ueda, Y., Akiyama, M., Ohta, K., & Miyaji, T. 2003, ApJ, 598, 886
Vandame, B. 2002, Proc. SPIE, 4847, 123
Veilleux, S., Rupke, D. S. N., Kim, D.-C., et al. 2009, ApJS, 182, 628
Werner, M. W., Roellig, T. L., Low, F. J., et al. 2004, ApJS, 154, 1
Worsley, M. A., Fabian, A. C., Barcons, X., et al. 2004, MNRAS, 352, L28
Worsley, M. A., Fabian, A. C., Bauer, F. E., et al. 2005, MNRAS, 357, 1281
Wright, E. L., Eisenhardt, P. R. M., Mainzer, A. K., et al. 2010, AJ, 140, 1868
Wuyts, S., Labbé, I., Schreiber, N. M., et al. 2008, ApJ, 682, 985